Article

Z-Scheme Heterojunction of 3-Dimensional Hierarchical Bi_3O_4Cl/Bi_5O_7I for a Significant Enhancement in the Photocatalytic Degradation of Organic Pollutants (RhB and BPA)

Syed Taj Ud Din [ID], Hankyu Lee and Woochul Yang *

Department of Physics, Dongguk University, Seoul 04620, Korea; tajuddins.phy@gmail.com (S.T.U.D.); lhk0022@naver.com (H.L.)
* Correspondence: wyang@dongguk.edu; Tel.: +82-222-603-444

Abstract: In this study, we report the synthesis of a 3-dimensional (3D) hierarchical Bi_3O_4Cl/Bi_5O_7I (BOC/BOI) heterostructure for the photocatalytic degradation of Rhodamine-B (RhB) dye and colorless Bisphenol-A (BPA) pollutant under visible light. The heterostructure was prepared using in situ solvothermal and calcination methods. BOC/BOI exhibits a 3D hierarchical structure constructed with thin nano-platelets. The photocatalytic performance of the BOC/BOI photocatalyst demonstrated that the degradation efficiencies of RhB and BPA were 97% and 92% after light illumination within 90 and 30 min, respectively. In comparison, bare BOC and BOI efficiencies were only 20% and 10% for RhB dye, respectively, and 2.3% and 37% for BPA aqueous pollutants, respectively. Moreover, radical trapping measurements indicated that $\bullet O_2^-$ and $\bullet OH$ radicals played prominent roles in RhB and BPA degradation into mineralization. Analysis of band structures and photochemical redox reactions of BOC/BOI revealed a Z-scheme charge transfer between BOC and BOI by an internal electric field formed at the interface. Therefore, the highly improved photocatalytic performance of the BOC/BOI heterostructure is attributed to the synergetic effects of large surface area, high visible-light absorption, and the enhanced separation and transport of photo-excited electron–hole pairs induced by the hierarchical and Z-scheme heterojunction of the BOC/BOI.

Keywords: 3D-hierarchical morphology; Z-scheme Bi_3O_4Cl/Bi_5O_7I heterojunction; photocatalytic degradation; organic pollutant; visible-light absorption

1. Introduction

As water pollutants have become an increasingly severe threat to life in this industrialized society, removing hazardous pollutants is currently a major social challenge. The pollutants mostly included in water are hazardous organic dyes and phenolic compounds. Rhodamine-B (RhB) is a common water-soluble organic dye used widely in various industry fields. Since it is classified as carcinogenic and neurotoxic, it poses health risks to humans [1]. Thus, its maximum allowable concentration is in the range from 14 to 140 µg/L in water [2]. Other than dyes, the colorless Bisphenol-A is the other frequently used compound. It is also a widely used raw material for the fabrication of numerous polymeric materials [3]. Its no-effect concentration is required to be less than 0.06 µg/L because its long-term exposure causes endocrine-based, neurological, and reproductive developmental disorders [4]. Therefore, the removal of RhB and BPA from the wastewater is crucial before discharging into water reservoirs and landfills. In general, adsorption through microbial treatment and chemical redox reaction has been used to remove these pollutants. However, these approaches have some limitations, due to low efficiency, high cost, and incomplete removal of contaminants [5]. Therefore, the effective elimination of these hazardous organic pollutants from wastewater remains a challenge.

To solve these issues, photocatalysis has attracted substantial attention due to environmental friendliness and its use of freely available solar light [6–8]. The photocatalytic process of a semiconductor consists of the absorption of photons, the separation and transport of photo-excited charge carriers, and the redox reaction on the surface. Although various semiconducting photocatalysts with high photocatalytic performance have been reported, there are still some limitations, such as high electron–hole recombination, inappropriate redox potentials, and low capability of visible-light absorption [9]. In particular, to enhance the separation and transport of photo-excited charge carriers, which is a key process during the photocatalytic process, various strategies have been explored including nonmetal doping [10], the deposition of noble or non-noble metal as a cocatalyst on the semiconducting photocatalyst [11–14], type-II heterojunction [15], and Z-scheme heterojunction photocatalyst [16] through the coupling of two semiconducting materials.

The Z-scheme heterojunction photocatalyst has attracted extensive attention due to the direct transfer and spatial separation of photogenerated charge carriers between two photocatalysts, and maintaining its high redox ability of both surfaces [17]. Various nanocomposites or heterojunctions, such as MoS_2/Bi_2WO_6, $g-C_3N_4/WO_3$, CdS/Bi_3O_4Cl, etc. [13–15], have been used to synthesize Z-scheme photocatalysts for the degradation of aqueous organic pollutants. Recently, bismuth oxyhalides (BiOX (X = Cl, Br, I))-based nanocomposites are considered to be promising candidates for use as Z-scheme heterojunction photocatalysts. The layered crystal structure of BiOX composed of the [X]-[BiO]-[X] gives it unique electronic and structural properties, such as bandgap tunability [18], easy adjustment of conduction, and valence band potentials via the different compositions [19], formation of internal electric field between interlayers [20], and possible growth in multiple dimensions [21]. In particular, Bi_3O_4Cl (BOC) and Bi_5O_7I (BOI) are photochemically stable and have suitable bandgaps of 2.60 eV and 3.01 eV for visible-light absorption, respectively [22,23]. Furthermore, the more negative conduction band (CB) potential of BOI and the more positive valence band (VB) potential of BOC are ideal for the maximum generation of super-oxide ($^\bullet O_2{}^-$) and hydroxyl ($^\bullet OH$) radicals, respectively, which are beneficial for the degradation of organic pollutants [24].

Therefore, various Z-scheme heterostructures of the other group semiconductors combined with BOC or BOI have been developed for photocatalytic applications. For instance, Zhou et al. prepared a series of BOI/MIL-53(Fe) nanocomposites [6]. The well-matched energy levels of BOI with MIL-53(Fe) enabled the construction of a direct Z-scheme heterojunction for the degradation of RhB under visible-light irradiation. Similarly, Jiang et al. used a facial pH control route to develop a $BOC/Bi_{12}O_{17}Cl_2$ Z-scheme composite by the in situ growth of BOC on the surface of $Bi_{12}O_{17}Cl_2$ for high photodegradation efficiency under visible light [25]. In another study, Che et al. prepared a Z-scheme $BOC/g-C_3N_4$ heterostructure to remove antibiotics, dye, and heavy metal from water under visible light [26]. The high photocatalytic performance is attributed to the Z-scheme heterojunction and the strong interfacial functionalization between the BOC nano-flakes and the $g-C_3N_4$ nanosheets interface.

Meanwhile, the morphology of the photocatalyst strongly affects the photocatalytic performance. Therefore, various morphologies, such as zero-dimensional (0D) nanodots [27], 1D nanorods [28], 2D nanosheets [29], and 3D hierarchical [30,31] nanostructures, have attracted significant attention due to their high surface-to-volume ratio, which increases the amount of photoactive sites [32]. Use of the nanostructures with 3D hierarchical morphologies is a promising approach to develop efficient photocatalysts, as this design inhibits self-aggregation of nanostructures due to high surface energies. However, the photocatalytic performances of 3D hierarchical single semiconductors and conventional heterostructures are far from ready for implementation in the photocatalytic degradation of organic pollutants. Therefore, it is necessary to develop a 3D hierarchical Z-scheme heterostructure to benefit from the synergy of its high surface area, high electron–hole separation, and high redox ability.

In this study, we prepared a Z-scheme BOC/BOI heterojunction photocatalyst with a 3D-hierarchical morphology for enhancement in the photocatalytic degradation of RhB and BPA. The heterojunction was fabricated using an in situ two-step solvothermal-calcination method. Morphological characterizations show that BOC/BOI has a 3D-hierarchical structure constructed with thin nano-flakes. Analysis of energy-band structures of BOC/BOI heterojunction proves that the generation of an internal electric field directed from BOI to BOC facilitates Z-scheme charge transfer between BOC and BOI. Thus, the BOC/BOI demonstrated a higher reaction rate and degradation efficiency than the bare BOC and BOI during RhB and BPA degradation. Furthermore, the degradation pathway was suggested by identifying the mineralization and reaction intermediates using liquid chromatography–mass spectroscopy. The excellent performances of the BOC/BOI heterostructure are attributed to more active sites induced by its unique 3D hierarchical morphology and the enhancement of the separation of photogenerated electrons and holes through the Z-scheme transfer process. This research presents that the Z-scheme BOC/BOI heterojunction with a 3D-hierarchical structure is a suitable photocatalyst for the degradation of environmental pollutants.

2. Materials and Methods

2.1. Chemicals

Bismuth nitrate pentahydrate ($Bi(NO_3)_3 \cdot 5H_2O$, 99%), potassium chloride (KCl, 99%), potassium iodide (KI, 99%), ethylene glycol ($(CH_2OH)_2$, 99%), 1-Vinyl-2-Pyrrolidone (PVP) ((C_6H_9NO), 99%), Rhodamine-B ($CH_{31}ClN_2O_3$, 99%), Bisphenol-A ($C_{15}H_{16}O_2$, 99%), dimethylformamide (DMF), nitro-blue tetrazolium (NBT), terephthalic acid (TA) and 1,4-benzoquinone (BQ) ($C_6H_4O_2$, 99%) were purchased from Sigma Aldrich Inc. (St. Louis, MO, USA). ethanol (C_2H_5OH, 99%) and isopropyl alcohol (IPA) (C_3H_8O, 99%) were purchased from DAEJUN Co., Ltd. (Daejun, Korea). All reagents were used without any further purification.

2.2. Preparation of BOC/BOI Composites

An in situ two-step solvothermal method was used to prepare the BOC/BOI heterojunction, as shown in Figure S1. In Step (a), $Bi(NO_3)_3 \cdot 5H_2O$ (4.5 mmol) was dissolved in 15 mL of ethylene glycol (EG). The mixture was then sonicated and stirred vigorously for 30 min. In Step (b), the PVP (10 mmol) was dissolved in 10 mL of EG, which was then sonicated and stirred vigorously for 30 min. In Step (c), the PVP solution (prepared in Step (b)) was added dropwise into the $Bi(NO_3)_3 \cdot 5H_2O$ solution (prepared in Step (a)) and stirred for 15 min at 400 rpm. Next, in Step (d), various molar ratios of potassium chloride (KCl) and potassium iodide (KI) were dissolved in 10 mL of EG by stirring for 30 min. In Step (e), the KCl:KI solution was added dropwise into the $Bi(NO_3)_3 \cdot 5H_2O$ solution (prepared in Step (c)) under continuous stirring. In Step (f), the mixture was then transferred to a 50 mL Teflon-lined autoclave and sealed. Next, the autoclave was heated at 160 °C for 12 h and cooled naturally to room temperature. After that, the raw BOC/BiOI composite powder was isolated from the EG solution using centrifugation at a speed of 8000 rpm for 10 min and washed with distilled (DI) water and ethanol. The washed BOC/BiOI powder was then dried overnight at 60 °C and put into alumina crucibles. The powder was calcinated in a muffle furnace at 450 °C for 1 h with a ramp rate of 5 °C/min. As a result, the targeted BOC/BOI composites were prepared. The samples with various molar ratios of 1:1, 1:2, 1:3.3, and 1:4.6 of KCl and KI were synthesized, and these were respectively denoted as BOC/BOI-1, BOC/BOI-2, BOC/BOI-3, and BOC/BOI-4. In addition, for comparison, bare BOC and BOI samples were prepared with a similar method as the one used for BOC/BOI. For the preparation of bare BOC and BOI, KCl and KI were added relative to the molar ratio of Bi in $Bi(NO_3)_3 \cdot 5H_2O$ solution, such as Bi:Cl with 3:1 and Bi:I with 1:1.

2.3. Characterization of Prepared Samples

Structural analysis of the prepared samples was conducted using X-ray powder diffractometer (XRD)(Ultima IV, Rigaku Inc., Tokyo, Japan) with Cu-Kα as an X-ray source

(wavelength of 1.5409 Å) operated at a scan rate of 5°/min in the diffraction angle (2θ) range from 10° to 80°. The crystalline phase was characterized through Micro-Raman spectroscopy measurement (XperRAM100, Nanobase Inc., Seoul, Korea), equipped with a green laser source (wavelength of 532 nm and power of 6 mW). The morphology and elemental compositions were examined using a field emission scanning electron microscope (SEM) (JSM-6700F, JEOL Ltd., Tokyo, Japan) equipped with an Energy-dispersive X-ray spectroscope (EDX). A UV-visible spectrophotometer (V-750, Jasco Inc., Tokyo, Japan) equipped with a 60 mm integrating sphere was used to investigate the optical properties, including the diffuse reflectance spectrum and optical bandgap. X-ray photoemission spectroscopy (XPS) (Veresprobe II, ULVAC-PHI Inc., Kanagawa, Japan) with a Monochromatic Al Kα X-ray source was used to examine the chemical composition of samples. The collected XPS data were calibrated with a non-oxygenated carbon peak that originated at 284.8 eV [30,31]. The photoluminescence (PL) spectra of the samples were obtained using fluorescence spectrophotometer (Fp-8600, Jasco Inc., Tokyo, Japan) with an excitation wavelength of 330 nm. The time-resolved photoluminescence (TRPL) decay spectra were obtained using Spectrofluorometer (FS5-TCSPC, Edinburgh Instruments Ltd., Edinburgh, UK) using 375 nm picosecond pulsed laser diode (EPL-375) as an excitation source. The TG/DTA analyzer (STA 6000, Perkin Elmer, Waltham, MA, USA) was used to collect the thermo-gravimetric analysis (TGA) and differential scanning calorimetric (DSC) data of the synthesized samples (Figure S2). The microstructures of the samples were analyzed using high-resolution transmission electron microscopy (HRTEM: Talos F200X TEM, FEI Co., Hillsboro, OR, USA) operated at an accelerating voltage of 200 kV. The Gatan microscopy software (digital micrograph™, version 3.7.4, GATAN Inc., Pleasanton, CA, USA) was used to obtain fast Fourier transform (FFT), inverse fast Fourier transform (IFFT), and TEM line profile from the HRTEM images.

2.4. Photocatalytic Activity Measurements

The photocatalytic characteristics of the samples were determined using a visible light source with a 300 W Xenon lamp (1000 W/m^2) (CEL-HXF300, CEAULIGHT Co., Beijing, China) equipped with a UV-IR cutoff filter (420 nm > λ > 780 nm). RhB dye and BPA colorless pollutants were used to evaluate the degradation efficiency of the synthesized photocatalysts. The pollutant aqueous solution in a double wall jacket beaker (80 cm^2 surface area) connected with a water chiller was kept perpendicular to the light source at a distance of 30 cm. Each photocatalyst with 10 mg and 40 mg was used to degrade 40 mL of RhB dye (17 ppm) and BPA colorless pollutant (15 ppm), respectively. Initially, the RhB and BPA solution was stirred for 60 min and 30 min, respectively, under the dark condition to attain adsorption-desorption equilibrium of the photocatalysts. Next, after a specific time interval, a 2 mL solution was taken from each solution, which was then centrifuged for 3 min at 3000 rpm to separate the solution from the photocatalyst. The absorbance spectrum of the separated solution was determined using a UV-visible spectrophotometer, which established the rate of degradation to light irradiation time. Radical trapping experiments were conducted to determine the radical's dominant species involved in the photocatalytic decomposition of RhB. IPA, BQ, and KI of 2 mmol were used as trapping reagents to determine the active species such as $^{\bullet}O_2{}^-$, $^{\bullet}OH$ radicals and holes, respectively. NBT (0.025 mmol) was used as an indicator to determine the amount of $^{\bullet}O_2{}^-$ radical. We also employed a liquid chromatography–mass spectrometry (LC–MS) system (Agilent 6460 Triple Quad LC/MS, Agilent technologies Inc., Santa Clara, CA, USA), installed with a column (ZORBAX SB-C18 18 μL, 2.1 × 50 mm^2) for the degradation pathway and reaction intermediates investigation.

2.5. Electrochemical Impedance Spectroscopy Measurements

The electrochemical impedance spectroscopy (EIS) analysis was conducted on a three-electrode workstation (VSP Potentiostat, Biologic, Seyssinet-Pariset, France). The Pt-spiral wire and standard calomel were used as counter and reference electrodes, respectively. An

aqueous solution of 0.5 M Na_2SO_4 (50 mL) was used as an electrolyte. A clean fluorine-doped tin oxide (FTO) glass was employed as a substrate of the working electrode. The working electrode was prepared from the slurry, which was made by dispersing the photocatalyst (0.1 mg) in DMF (1 mL), then sonicated for an hour. The slurry was coated over the FTO by a drop-casting technique and dried at 160 °C for 1 h before being used as a working electrode.

3. Results and Discussion

3.1. Structural, Morphological, and Elemental Characterization

The structural phases of the BOC, BOI, and BOC/BOI-3 were analyzed using XRD patterns, as shown in Figure 1a. The XRD pattern of the prepared BOC was well matched with the monoclinic characteristic of BOC (PDF#36-0760) [33]. Similarly, the XRD pattern of the prepared BOI was the same as the orthorhombic phase of BOI (PDF#040-0548) [34]. The characteristic peaks of BOC and BOI were found to co-exist in the XRD patterns of BOC/BOI-3 samples. Furthermore, the XRD pattern of BOI exhibited an intense and robust peak at 28.08°, which confirmed the preferential growth of BOI in the (312) plan. In addition, the XRD pattern of BOC exhibited a broad peak at 29.64°, which confirmed the growth of BOC in the (411) plan. These results provide evidence that the targeted phase of the composite was synthesized successfully.
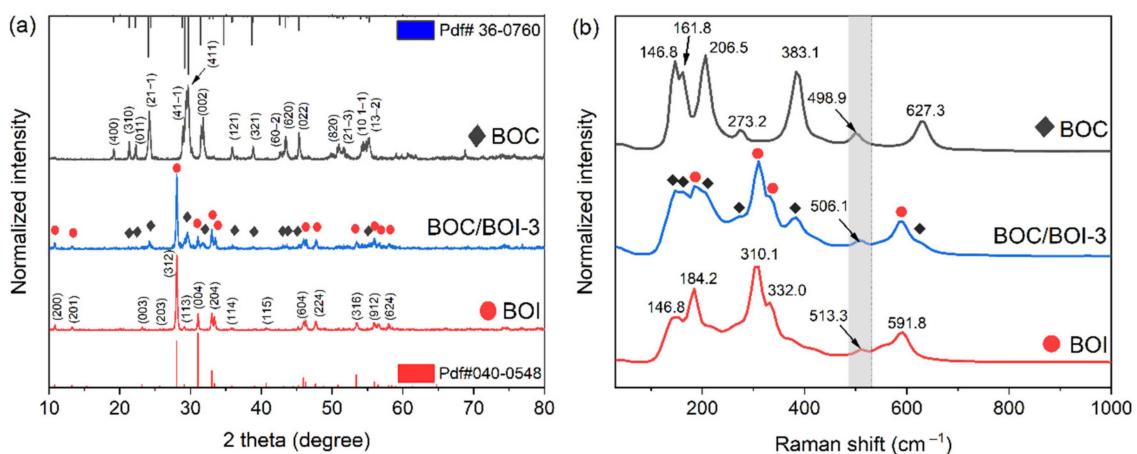

Figure 1. (**a**) XRD patterns and (**b**) Raman spectra of BOC, BOI, and BOC/BOI-3 heterostructure photocatalysts.

The structural characteristics of the BOC, BOI, and BOC/BOI-3 were further analyzed using Raman measurements, as shown in Figure 1b. For BOC, a peak at 146.8 cm^{-1} corresponds to A_{1g} vibration originating from the stretching mode of the Bi-Cl bond [35], while the remaining peaks between 161.8 cm^{-1} to 627.3 cm^{-1} correspond to the Bi-O bond vibration [36]. For BOI, the peak at 146.8 cm^{-1} indicates E_{1g} vibration due to the internal stretching mode of Bi-I [37]. The higher-frequency peaks observed between 184.2 cm^{-1} and 591.8 cm^{-1} are related to Bi-O bonding, which are generated due to the oxygen-rich environment in BOI [38,39]. Furthermore, the presence of BOC and BOI characteristic peaks in the Raman spectra of BOC/BOI-3 verified the successful formation of a BOC/BOI heterostructure. In addition, although the positions of all observed peaks in the heterostructure are similar to the BOC and BOI samples, the peak at 506.1 cm^{-1} in the BOC/BOI-3 composite is blue-shifted and red-shifted compared to BOI and BOC, respectively. These shifts indicate that BOI and BOC in the BOC/BOI-3 composites are strongly interconnected due to the interfacial interaction between oxygen and bismuth atoms.

To investigate the morphology and microstructure of the synthesized samples, FESEM and TEM measurements were performed. Figure 2 shows SEM images of the BOC, BOI, and BOC/BOI-3 samples. The morphology of BOC was observed to be irregularly agglomerated

nanoparticles of about 80 nm in size (Figure 2a,b). By contrast, SEM images of the BOI show micro-spherical structures composed of elongated nanoparticles with an approximate thickness of 100 nm (Figure 2c,d). In comparison, the SEM images of BOC/BOI-3 show micro-spherical structures composed of nano-platelets with an average thickness of 50 nm (Figure 2e,f). The nano-platelets of the BOC/BOI-3 are thinner than those of BOC and BOI.
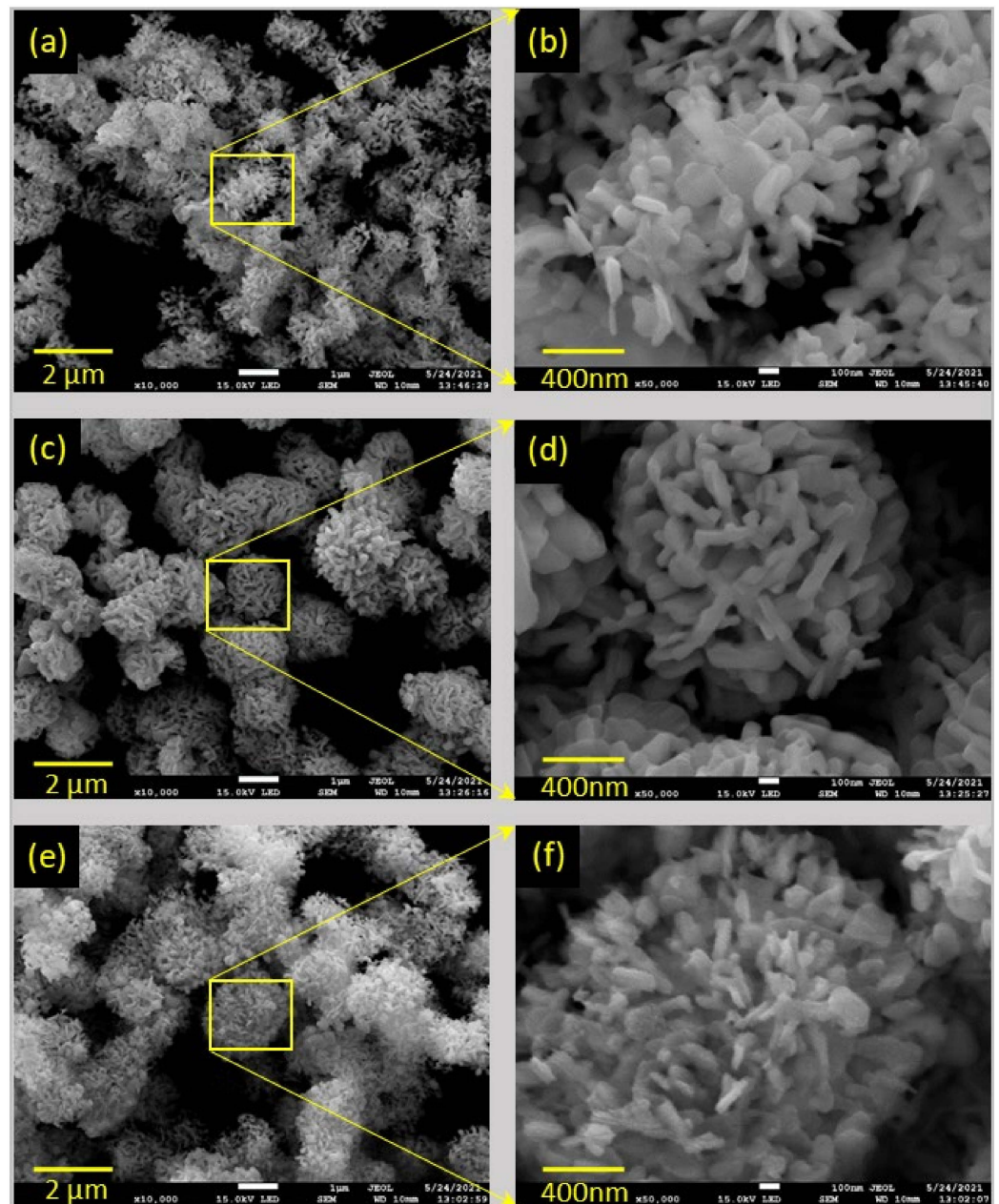

Figure 2. FESEM images of (**a**,**b**) BOC, (**c**,**d**) BOI, and (**e**,**f**) BOC/BOI-3 heterostructures.

The microstructure of the BOC/BOI heterojunction was investigated using HRTEM. Figure 3a reveals that BOC/BOI-3 composite has a 2D nano-platelets morphology with sizes varying from 50 nm to 300 nm. The HRTEM image of the yellow rectangle region marked in Figure 3a shows that 2D nano-platelets of BOC are grown on the surface of BOI (Figure 3b). A small portion (enclosed in a red rectangle in Figure 3b) is taken to obtain the IFFT pattern, as shown in Figure 3c. The intensity line profiles of the planes observed from IFFT patterns are shown in Figure S3a,b, respectively. The fringe spacings of the perpendicular planes of BOC and BOI are determined to be 0.410 nm and 0.507 nm, respectively. According

to the XRD reference file (PDF#36-0760), these measured fringe spacings correspond to the (011) and (400) planes of BOC in Figure 3c, respectively. Similarly, a small portion (enclosed in a white rectangle in Figure 3b) is taken to determine the IFFT pattern for bare BOI, as shown in Figure 3d. The intensity line profiles of these oriented planes are defined with a fringe spacing of 0.315 nm (Figure S3c), which corresponds to the (312) plan of BOI according to the XRD reference file (PDF#040-0548). Altogether, the TEM analysis confirms the successful coupling of BOC with BOI, as illustrated in Figure 3e. The elemental composition of BOC/BOI-3 is confirmed by EDS mapping of the region in Figure S4a, as shown in Figure S4. The sum EDS image shows the uniform distribution of the corresponding elements (Figure S4b). The elemental mapping of individual Bi, O, Cl, and I clearly show that each element is uniformly distributed (Figure S4c–f). In addition, the EDS spectrum indicates that the Bi, O, Cl, and I contents are about 44.66%, 44.25%, 4.34%, and 5.03%, respectively, as listed in the inset table of Figure S4g.
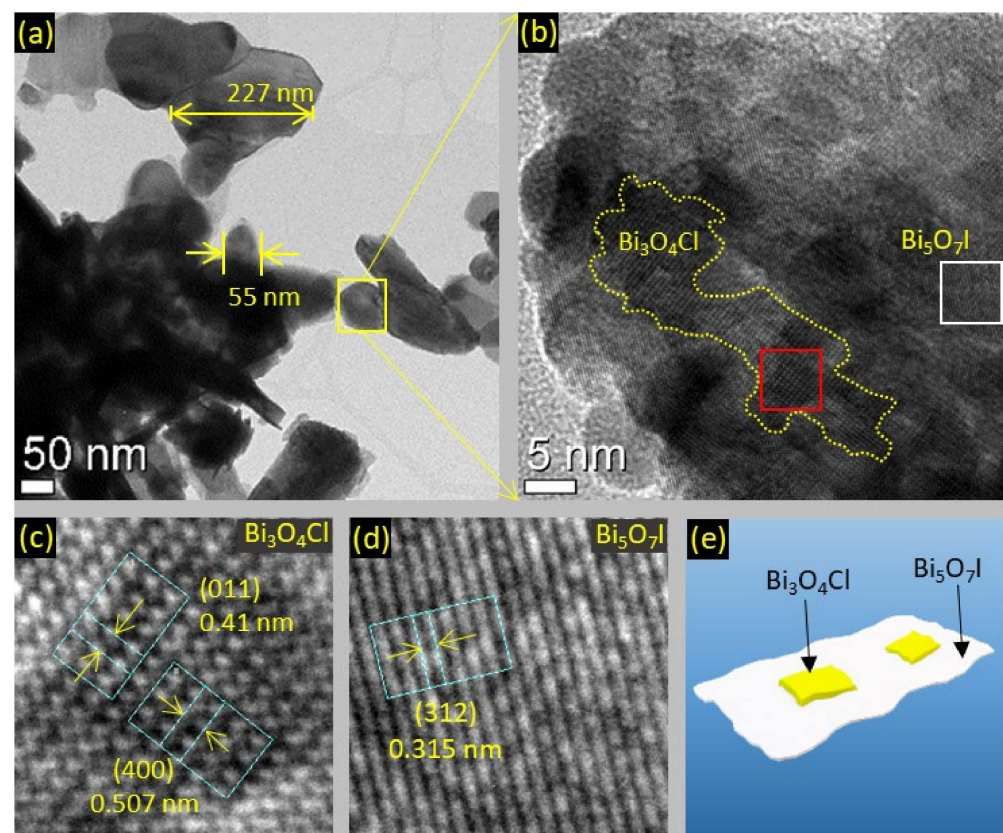

Figure 3. HRTEM images of (**a**,**b**) BOC/BOI-3 nano-platelets, (**c**) IFFT pattern of BOC and (**d**) BOI in BOC/BOI, and (**e**) schematic of BOC/BOI-3 heterostructure.

Moreover, the elemental compositions of BOC, BOI and BOC/BOI-3 were further investigated using XPS. The survey XPS spectrum of the BOC/BOI-3 composite shows the presence of O 1s, I 3d, Cl 2p, and Bi 4f peaks, thus confirming the existence of BOI and BOC in the composite (Figure S5). Meanwhile, the C1s peak observed at 284.800 eV originates from the carbon tape used as a substrate for XPS measurements [40,41]. The Bi 4f XPS spectra of all samples exhibit the typical peaks of Bi $4f_{5/2}$ and Bi $4f_{7/2}$, which are attributed to the Bi-O bonding (Figure 4a). Both peaks of BOC/BOI shift to lower binding energies (0.300 eV and 0.425 eV) than BOC and higher binding energies (0.325 eV and 0.200 eV) than BOI. The O 1s spectra of each sample were deconvoluted into two peaks, as shown in Figure 4b. The main peak at the lower binding energy and the satellite peak at the higher binding energy originate from Bi-O and adsorbed oxygen, respectively [42]. In particular, the position of the main peak in BOC/BOI is lower than that in BOC and higher than that

in BOI [43], which is similar to the tendency of the Bi 4f spectra. We also compared the I 3d spectrum of BOI and the Cl 2p spectrum of BOC with the BOC/BOI composite, as depicted in Figure 4c,d. Figure 4c shows the I 3d spectra of the BOI and BOC/BOI-3 samples [44]. It can be seen that a more oxygenated environment was generated in the form of composite. Therefore, the position of both the I $3d_{1/2}$ and I $3d_{5/2}$ peaks in the composite were shifted by 0.075 eV toward a higher binding energy than BOI. The blue shift may result from a more oxygenated environment in the composite. In the Cl 2p spectrum in Figure 4d, the deconvoluted Cl $2p_{1/2}$ and Cl $2p_{3/2}$ peaks of the Cl 2p peak in the composite were also shifted by 0.300 eV and 1.000 eV toward a lower binding energy than BOC, respectively.
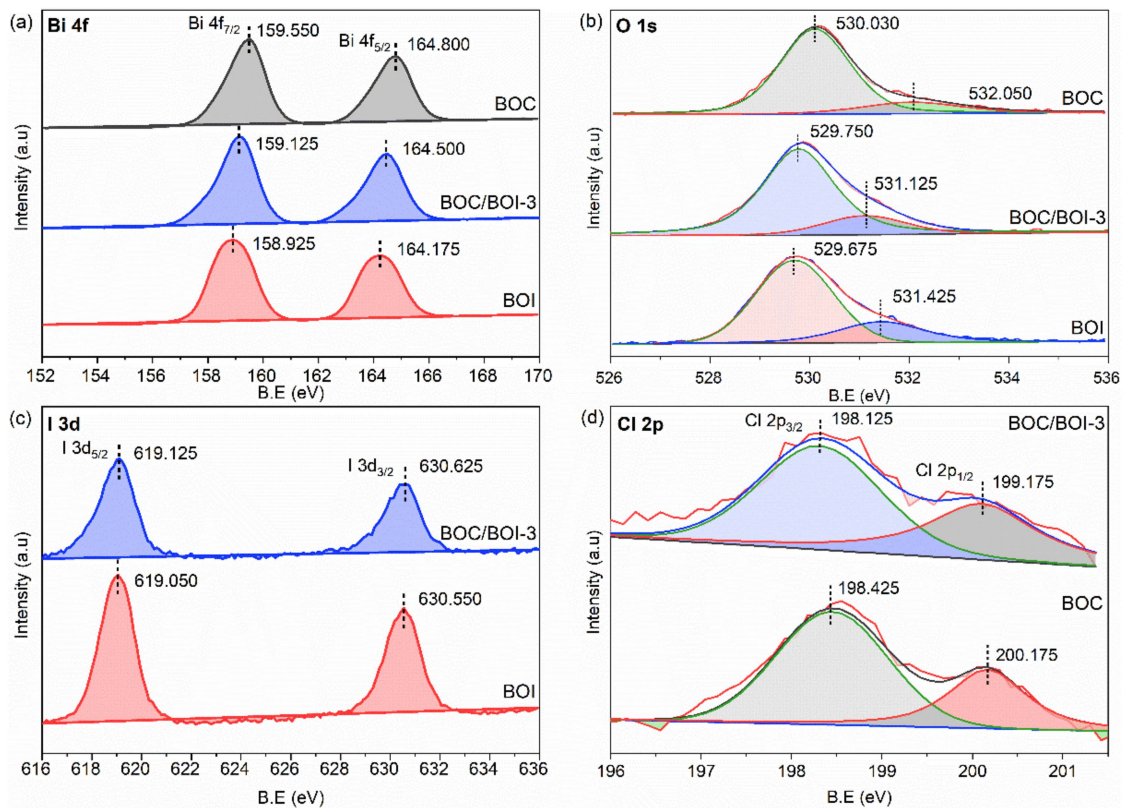

Figure 4. (**a**) High-resolution XPS core level data for Bi 4f, (**b**) O 1s, (**c**) I 3d, and (**d**) Cl 2p obtained from BOC, BOI, and BOC/BOI-3 samples.

In XPS analysis, it is observed that all peak positions of BOC/BOI composite were shifted toward higher and lower binding energies than BOI and BOC, respectively. Since Iodine (I) is less electronegative than chlorine (Cl), it is easy for I to leave electrons. Theoretically, when I donate electrons, the concentration of the outer shell's electron decreases, resulting in a reduced shielding effect and corresponding to an increase in the binding energy of the inner electrons. As a result, the corresponding XPS peaks shift toward a high binding energy. Therefore, this high energy shift indicates the electron density migration from BOI to BOC in the BOC/BOI-3 heterojunction. The vice versa effect is responsible for the shift of the BOC peaks to lower binding energies.

3.2. Photocatalytic Performance, Elucidation of Active Species, and Degradation Pathway

The photocatalytic performances of the BOC, BOI and BOC/BOI samples were evaluated by degrading RhB dye and BPA colorless pollutant in an aqueous solution under visible-light irradiation, as shown in Figure 5. Figure 5a shows that the degradation ratio (C/C_o) of RhB dye solution over BOC/BOI composites is substantially higher than that of pure BOC and BOI. Specifically, the BOC/BOI-3 and BOC/BOI-2 composites completely decomposed RhB dye solution within 160 and 220 min, respectively. The temporal absorp-

tion spectra of RhB dye solution with BOC/BOI-3 show a gradual decrease in absorbance intensity with irradiation time (Figure S6). Eventually, the absorbance peak completely disappears after 160 min, indicating complete decolorization of RhB dye. Furthermore, during photocatalytic degradation, the position of the peak shifts from 554.5 nm to 498.5 nm, which is caused by the deethylation of the RhB dye [45].
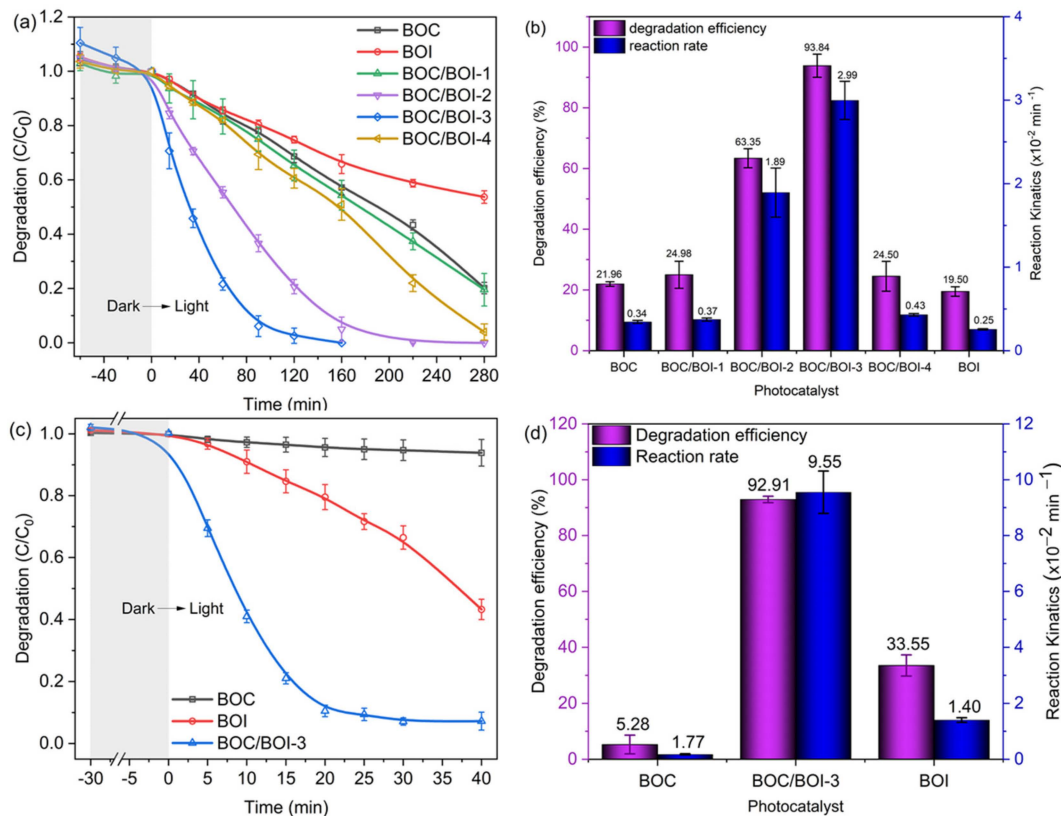

Figure 5. (**a**) Photocatalytic degradation of RhB and (**b**) degradation efficiency of RhB with the reaction rate constants employed by all samples; (**c**) Photocatalytic degradation of BPA and (**d**) its degradation efficiency with reaction rate constants employed by BOI, BOC and BOC/BOI-3 samples.

Furthermore, the degradation rate of the RhB solution in the presence of each sample can be calculated using the pseudo-first-order kinetic model, as expressed in Equation (1),

$$ln\frac{C_0}{C} = kt \tag{1}$$

where k, C_0, and C represent the reaction rate constant, initial concentration, and the remaining concentration of RhB in the solution at light-exposed time t, respectively. We obtained the k of each sample via curve fitting with Equation (1) (Figure S7). The obtained reaction rate and degradation efficiency for each sample are shown in Figure 5b. BOC/BOI-3 had the highest degradation rate of 0.040 min^{-1} as well as the highest degradation efficiency of 97.68% after 90 min of light irradiation. In addition, the photocatalytic performances of BOC, BOI and BOC/BOI-3 were evaluated by decomposing the BPA in an aqueous solution under visible light (Figures 5c,d and S8). The degradation efficiency of BOC/BOI-3 over BPA was ~92.89% within 30 min, which was much higher than those of the BOC and BOI samples. The degradation rate of BOC/BOI-3 was 0.094 min^{-1}, which was 120 and 6 times higher than those of bare BOC and BOI, respectively. Moreover, we compared the degradation performance of our synthesized sample with previously reported bismuth oxyhalide-based heterostructures and other bismuth-based heterostructures, as shown in Tables S2 and S3. Importantly, our grown BOC/BOI-3 sample exhibits a high degradation

rate and efficiency for both RhB and BPA under visible-light illumination, compared to the reported literature.

Next, radical trapping analysis was conducted to explore the active radicals generated in the BOC/BOI-3 sample during RhB degradation, as shown in Figure 6. BQ, IPA, and KI were used as trapping agents for $^\bullet O_2^-$, $^\bullet OH$, and h^+, respectively. Figure 6a depicts the degree of suppression of RhB degradation in the presence of BQ, IPA, and KI scavengers. The degradation of RhB in the presence of IPA is higher than those of BQ and KI. The corresponding degradation efficiency of RhB was reduced from 97% (no scavenger) to 54%, 46%, and 40% with IPA, BQ, and KI, respectively (Figure S9a). Next, Figure S9b shows that the degradation of RhB followed the first-order reaction kinetic model, wherein the degradation rate was reduced from 0.0400 min^{-1} (no scavenger) to 0.008, 0.007, and 0.005 min^{-1} with IPA, BQ, and KI, respectively. Thus, the results indicate that $^\bullet OH$, $^\bullet O_2^-$ radical, and h^+ can be generated during RhB degradation [46].
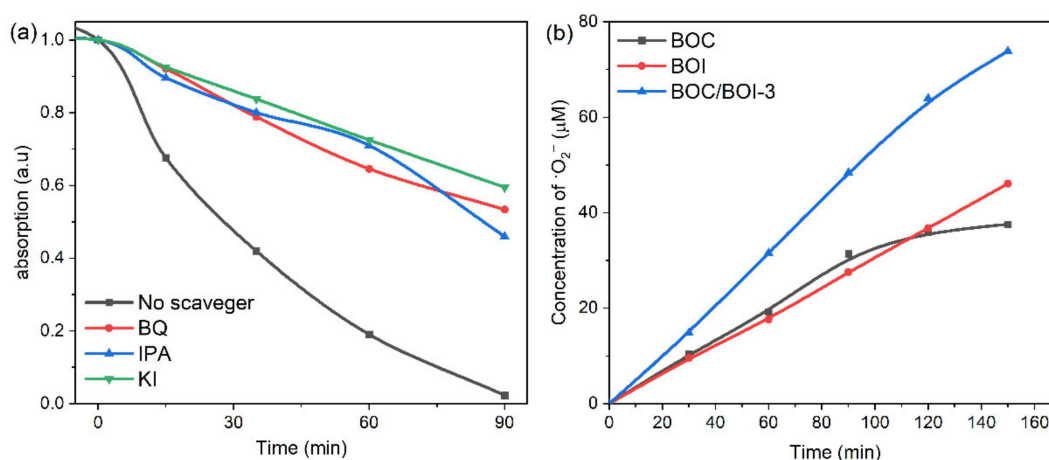

Figure 6. (**a**) Radical trapping experiments during degradation of RhB over BOC/BOI-3, (**b**) time-dependent concentration plots of the amount of $^\bullet O_2^-$ radicals.

To confirm the direct formation of each radical during RhB degradation, we employed NBT as a probe molecule for the detection of the $^\bullet O_2^-$ radical. To directly investigate the $^\bullet O_2^-$ radical, the temporal absorption spectra of NBT with UV light were obtained in the presence of the BOC, BOI, and BOC/BOI-3 samples, as shown in Figure S10. Please note that the decrease in UV absorbance at the main peak at 259 nm indicates the generation of $^\bullet O_2^-$ radicals during the transformation from NBT to Formazan [47]. Compared to BOC and BOI, BOC/BOI-3 has the lowest absorbance at 259 nm after 150 min, corresponding to the highest generation of $^\bullet O_2^-$ radicals (Figure S10a–c). Based on the reaction relationship between $^\bullet O_2^-$ and NBT (4:1 in molar ratio) (Figure S10d), the amount of $^\bullet O_2^-$ radicals can be calculated to be 37.6, 46.12, and 73.84 μmol/L after 150 min for BOC, BOI, and BOC/BOI-3, respectively (Figure 6b).

Finally, we performed LC–MS to elucidate the reaction intermediates, photocatalytic degradation pathway, and mineralization process of RhB and BPA over BOC/BOI-3 sample, as shown in Figure S11. It can be seen that the degradation products were measured at m/z = 443, 391, 354, 340, 251, 194, and 130 in Figure S11a. The possible degradation pathway and some relative degradation products can be proposed according to mass fragmentation results, as shown in Figure 7a. This result shows that as the photocatalytic reaction proceeds, the RhB molecules gradually divide into small molecules from m/z =443 to m/z =130 via N-deethylation and degradation of RhB chromophore structure. In the process of N-deethylation, the OH radicals will attack the central carbon of the RhB molecule with a high negative density charge, resulting in the degradation of RhB (m/z = 443) molecules into N-deethylated intermediates first (m/z = 391). Then, these N-deethylated intermediates (m/z = 391) are transformed into intermediates with the m/z value of 354 and 340 by

OH or O_2 radical attack on the bonding between benzene and chromophore, and further degraded into smaller m/z intermediates with the m/z value of 254, 251 and then to m/z 194 and finally convert to $m/z = 130$ on the cleavage of the chromophore. In Figure 7b, the systematic degradation pathway for BPA shows that the BPA molecules gradually convert into small molecules via two degradation routes. Rout (1) presents the BPA conversion into 4-n-octylphenol-mono-ethoxylate (m/z: 249) by attacking active radicals on the isopropyl/aliphatic chain between the two benzene rings. In rout (2), BPA converts into (m/z: 208), which may be allocated to the formation of 3 possible intermediates; (i) 1,1-di(p-toly)ethylene, (ii) 3,3-diphenylacrylaldehyde and (iii) 2-methyl-1,1diphenylpropene, and then converted into 4-isopropyle-3-methylphenol (m/z: 150) by the disconnection of two aromatic rings owing to redox reaction. Thereafter, the benzene ring opens with the oxidization resulting in the breaking of C–C bonds, leading to the formation of succinic acid (m/z: 118). Finally, it converts into smaller molecules, CO_2 and H_2O.
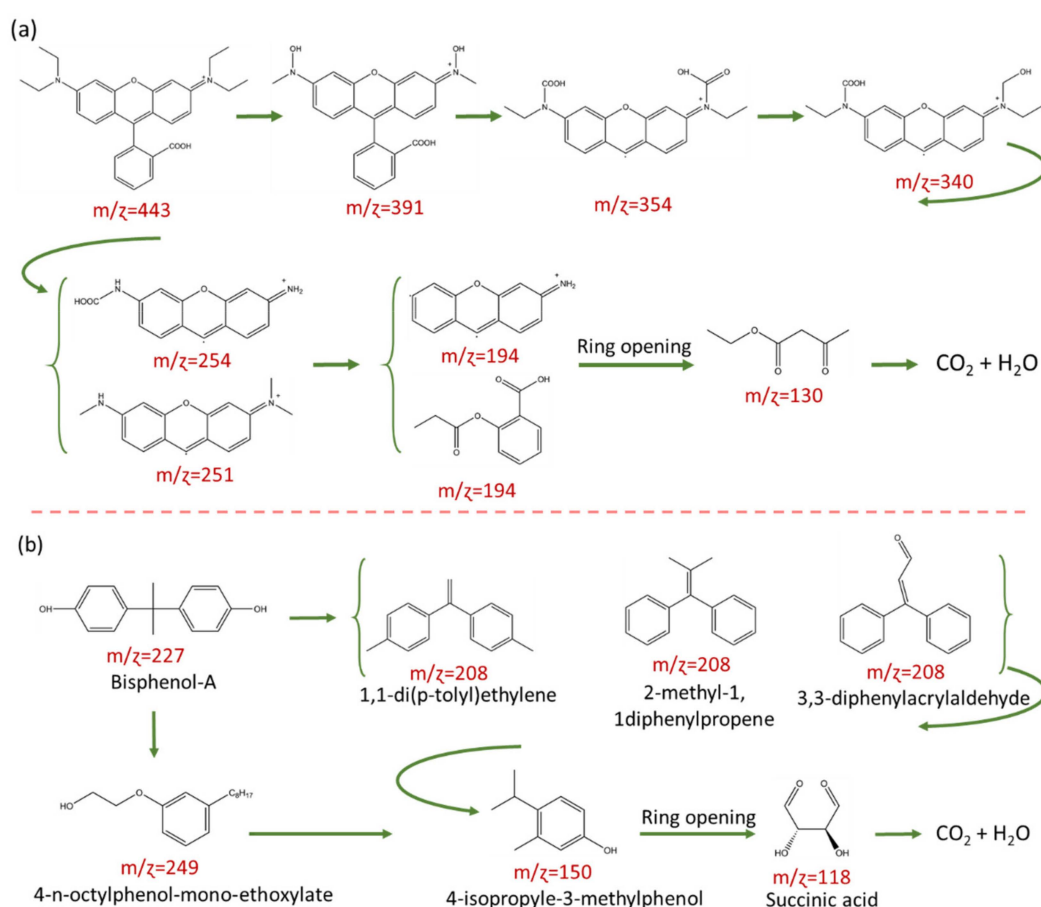

Figure 7. Photocatalytic degradation pathway and possible reaction intermediates in (**a**) RhB and (**b**) BPA over BOC/BOI-3.

3.3. Reusability, Structural and Morphological Stability of Photocatalyst

We further conducted the recycling experiments to evaluate the photocatlytic reusability and stability of BOC/BOI-3 heterojunction photocatalyst, as illustrated in Figure 8. It can be seen that BOC/BOI-3 provides 100% RhB degradation efficiency (Figure 8a) and 95% BPA degradation efficiency (Figure 8b) after the first cycle, while a subsequent decrease in catalytic activity is observed after the second and third run. After the 3rd cycle, 85.34% of RhB and 51.64% of BPA were degraded in 160 min and 40 min, respectively. The observed decrease in efficiency is probably caused by the adsorption of organic intermediates on the catalyst surface [48]. Therefore, the structural and morphological stability of BOC/BOI-3 was verified using XRD, Raman, and SEM for the BOC/BOI-3 after the

recycling experiment. In Figure 8c and Figure S12, we observed negligible variation in the XRD pattern and morphology, confirming structural and morphological stability. Additionally, the BOC/BOI-3 sample shows robust Raman intensity in a wide range because of the adsorption of the RhB molecule on the surface of BOC/BOI-3, which also reduced its photocatalytic performance in the 2nd and 3rd cycle during photocatalytic degradation (Figure 8d). However, no extra peak is observed in the Raman spectra of BOC/BOI-3 after degrading BPA due to the low concentration and less intense Raman active modes of BPA in the 125–1000 cm^{-1} range [49].
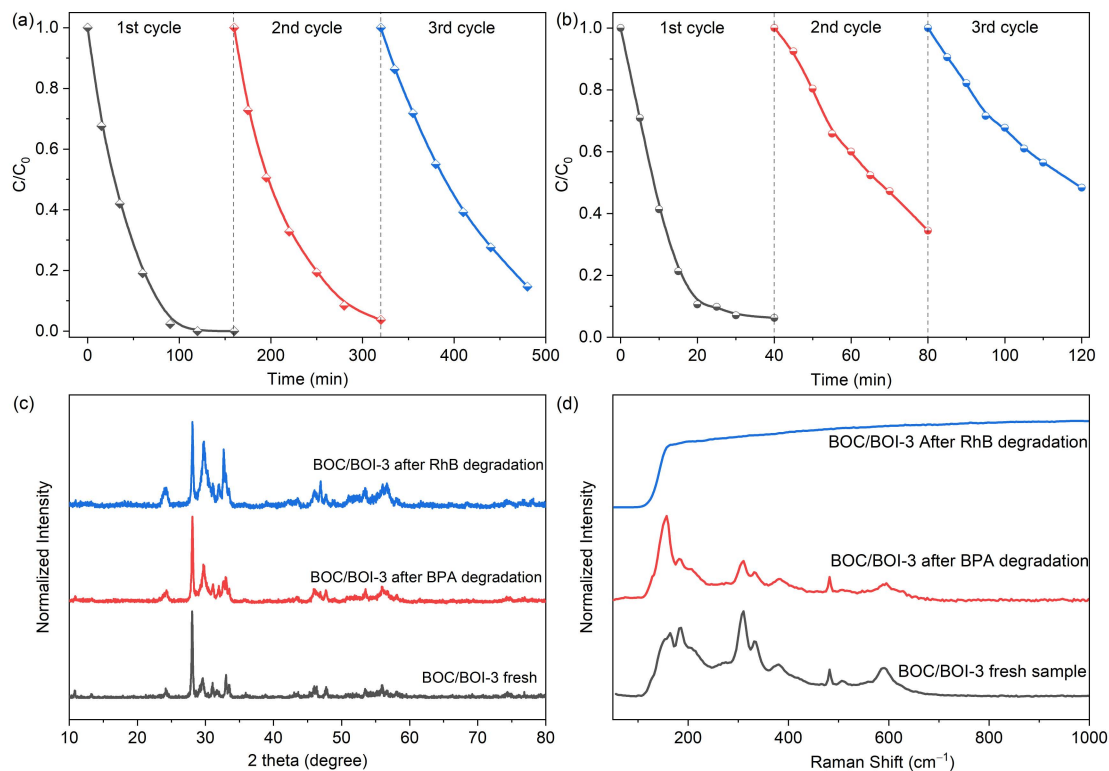

Figure 8. (**a**) Cyclic degradation test of Rhodamine-B and (**b**) Bisphenol-A over BOC/BOI-3 sample, (**c**) XRD pattern and (**d**) Raman spectra of BOC/BOI-3 sample before and after BPA and RhB degradation.

3.4. Behavior of Photogenerated Charge Carriers

PL measurements were conducted to investigate the recombination behavior of photo-induced e^{-}-h^{+} pairs in BOC, BOI, and BOC/BOI-3, as shown in Figure 9a. The BOC/BOI-3 composite exhibited a lower PL emission intensity than BOC and BOI, which indicates the reduced recombination of e^{-}-h^{+} pairs in the BOC/BOI-3 sample. Furthermore, we adapted time-resolved photoluminescence spectroscopy (TRPL) to estimate the lifetime of the excited charge carriers (Figure 9b and Table S1). The average lifetimes (τ_{avg}) of BOC/BOI-3 (8.80 ns) are longer than that of the BOC (7.42 ns) and BOI (7.91 ns). The longer τ_{avg} indicates that the recombination rate of the photogenerated charge carriers is reduced. Thus, the BOC/BOI composite led to more efficient separation of electron–hole pairs. We also measured the transient photocurrent response of the samples to examine the separation efficiency of the photo-excited charge carriers, as shown in Figure 9c. The BOC/BOI-3 has a higher photocurrent response than both the pristine BOC and BOI samples. The strong photocurrent response reveals the enhanced separation and transfer of the photogenerated charge carriers in the BOC/BOI composite. Next, an EIS Nyquist plot was taken to examine the electrode/electrolyte interfacial charge transfer resistance, as shown in Figure 9d. The Nyquist plot can be well-reproduced into solution-spreading resistance (R_s) and charge transfer resistance (R_{ct}), in parallel with the constant-phase element (CPE) (inset of Figure 9d) [50]. The R_{ct} values for BOC, BOI, and BOC/BOI-3

are 0.43, 0.64, and 0.32 MΩ, respectively. The smallest R_{ct} of BOC/BOI-3 has a lower charge transfer resistance than BOC and BOI. Therefore, these results suggest that the BOC/BOI-3 heterojunction can effectively suppress the recombination of photo-excited charge carriers, which will effectively improve the photocatalytic performance of the BOC/BOI-3 heterostructure.
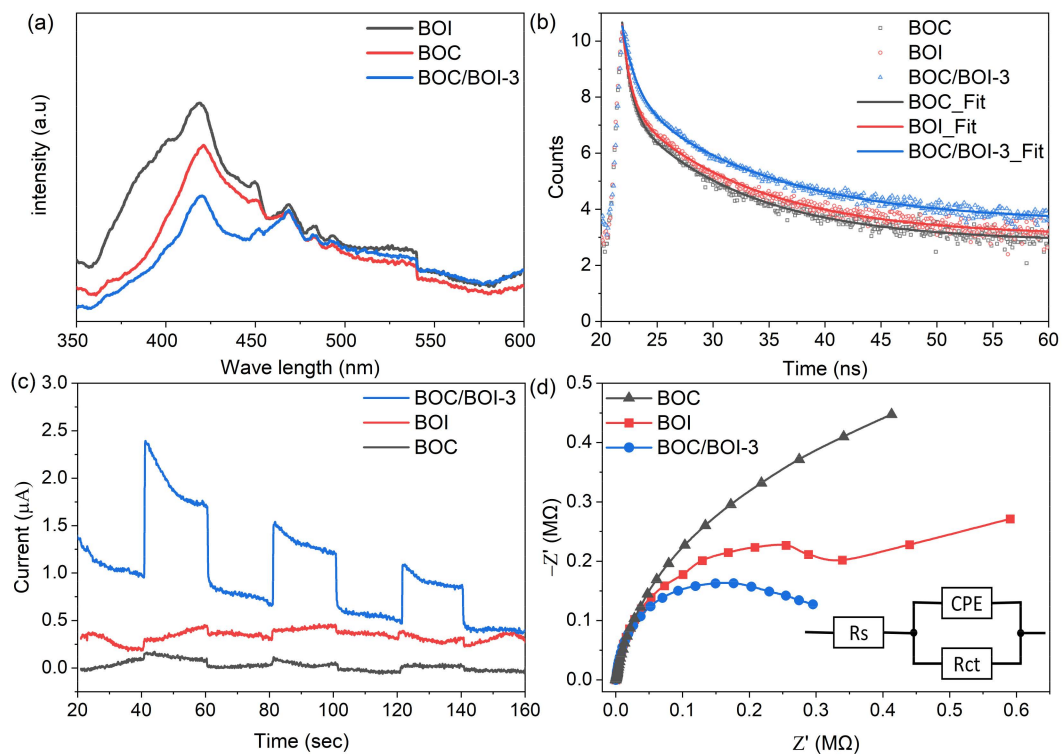

Figure 9. (**a**) Photoluminescence spectra, (**b**) TRPL decay spectra, (**c**), transient photocurrent response and (**d**) EIS Nyquist plots of BOC, BOI, and BOC/BOI-3 samples.

3.5. Photocatalytic Mechanism and Interfacial Charge Transfer Behavior

To elucidate the photocatalytic mechanism of the BOC/BOI heterostructure, the electronic structures of BOC, BOI, and BOC/BOI-3 were investigated through measurements of UV–Vis diffuse reflectance spectra (DRS), Mott–Schottky (MS) plots, and valence band (VB) XPS spectra, as shown in Figure 10. First, the UV–Vis DRS of BOC, BOI, and BOC/BOI-3 were measured to investigate optical absorption ability (Figure 10a). The absorption edges for the BOC and BOI were located at around 450 nm and 425 nm, respectively. In comparison, the absorption edge of the BOC/BOI-3 was extended to a longer wavelength of 460 nm. The extended absorption edge of BOC/BOI-3 is attributed to the strong contribution of BOC in BOC/BOI-3 to the absorption of visible light. Moreover, the optical bandgap of BOC and BOI could be obtained by curve fitting of Tauc plotting of $(\alpha h\nu)^n$ versus E_g (inset of Figure 10a), where n = 1/2 for the indirect band gap semiconducting behavior of BOC and BOI [51,52]. The obtained band gaps were 2.67 eV and 3.07 eV for BOC and BOI, respectively.
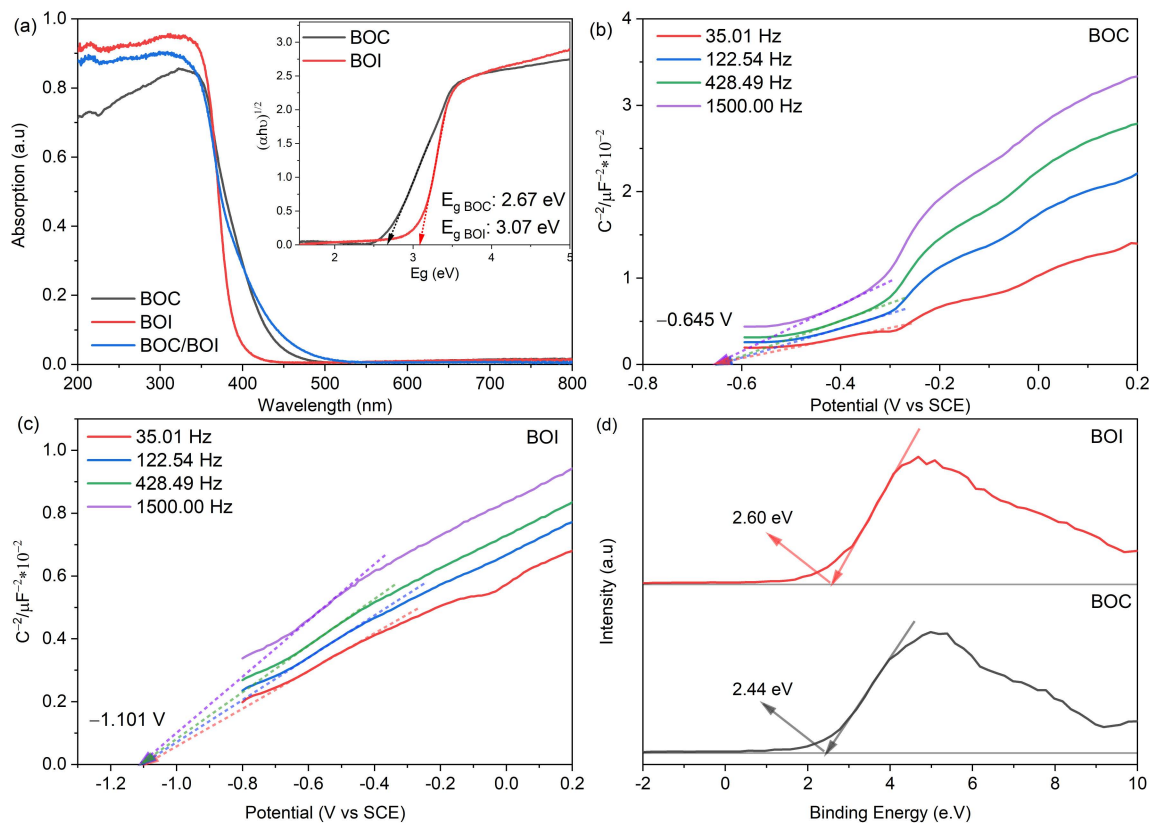
Figure 10. (**a**) UV–Vis diffuse reflectance spectra of BOC, BOI and BOC/BOI-3, (inset) showing Tauc plot of BOC and BOI, (**b**,**c**) Mott–Schottky plot of BOC and BOI, (**d**) Valence band XPS of BOC and BOI.

Second, the Fermi energy levels (E_f) of the prepared BOC and BOI samples were obtained using MS analysis, as shown in Figure 10b,c. The MS plots of BOC and BOI both show the positive slopes, thus indicating their n-type semiconducting behavior [53]. Furthermore, by extrapolating MS plots, the flatband potentials of BOC and BOI were obtained to be -0.645 V and -1.101 V vs. standard calomel electrode (SCE). Please note that the flatband potential (E_{fb}) of the n-type semiconductor represents the E_f level [54]. The E_f vs. normal hydrogen electrode (NHE) scale were calculated using Equation (2) [55]; as a result, the E_f of BOC and BOI were found to be -0.401 eV and -0.857 eV vs. NHE, respectively (Figure 11a).

$$E_{fb}\,(\text{vs. NHE}) \;=\; E_{fb}\,(\text{vs. SCE}) \;+\; 0.244(\text{eV}), \tag{2}$$

Furthermore, valence band (VB) XPS measurement was carried out to determine the VB potential for BOC and BOI, as shown in Figure 10d. The VB XPS spectra reveal the VB maxima of 2.44 eV and 2.60 eV for BOC and BOI, respectively. Thus, the VB potentials with respect to E_f level are calculated to be 2.039 V and 1.743 V vs. NHE for BOC and BOI, respectively (Figure 11a).

Furthermore, the CB minima of BOC and BOI were determined using the following Equation (3).

$$E_{CB}\,(\text{vs. NHE}) \;=\; E_{VB}\,(\text{vs. NHE}) \;-\; E_g, \tag{3}$$
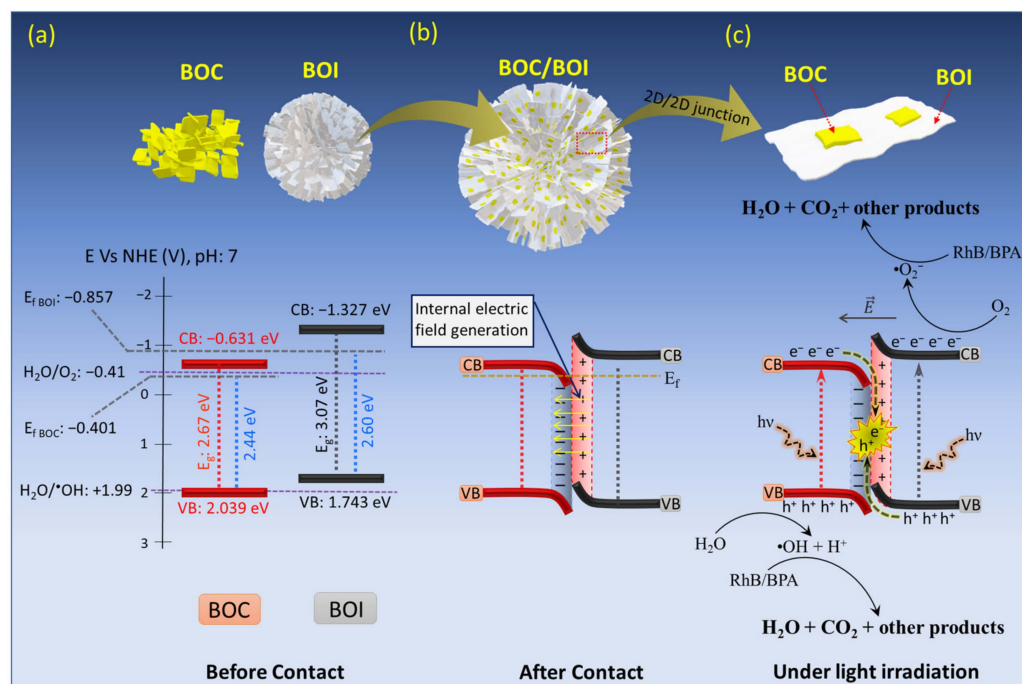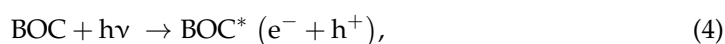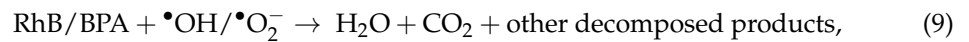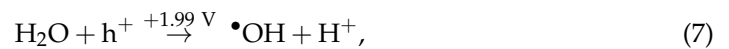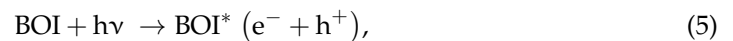
Figure 11. Schematics and energy-level diagrams of (**a**) BOC and BOI before contact, (**b**) IEF formation at BOC and BOI interface after contact, and (**c**) interfacial charge transfer behavior in BOC/BOI-3 heterostructure under visible-light irradiation.

where E_{CB}, E_{VB}, and E_g, denote the CB potential, VB potential and band gap of the sample, respectively. As a result, the calculated CB potentials for BOC and BOI are −0.631 V and 1.327 V vs. NHE, respectively (Figure 11a). Thus, based on the above analysis, the BOC/BOI will make a type-II heterojunction. When BOC and BOI formed the BOC/BOI heterojunction, the electrons would spontaneously migrate from BOI to BOC through the BOC/BOI interface to align the Fermi level because BOI has a higher E_f than BOC. The migration behavior of the charge carriers at the interface is also consistent with the elemental analysis in XPS spectra (as discussed in Section 3.1). This electron migration generates a depletion region at the BOC and BOI interface with an internal electric field (IEF) oriented from BOI to BOC, therefore resulting in the band bending upward for BOI and downward for BOC, respectively, as shown in Figure 11b.

Regarding the analysis of the band structure of the BOC/BOI-3 sample, a possible Z-scheme photocatalytic mechanism for BOC/BOI could be proposed (Figure 11c). Under visible-light irradiation, the charge carriers are excited simultaneously from the VB to the CB in both BOC and BOI to produce photogenerated e^- and h^+ (as shown in the below reactions (4) and (5)). Then, the photo-excited electrons in the CB of BOC will be easily transferred to the VB of BOI due to the IEF at the interface in the heterojunction; this initiates the Z-scheme charge transport of the photo-excited charge carriers in the photocatalytic processes (reaction (6) and in Figure 10c). As a result, the remaining photogenerated holes in the VB of BOC with strong oxidation ability will split H_2O into $^\bullet OH$ and hydrogen ions (H^+) (reaction (7)) due to the fact that the VB of BOC (2.039 eV) is more positive than +1.99 eV ($H_2O/^\bullet OH$ vs. NHE). At the same time, the remaining photogenerated electrons in the CB of BOI will reduce the O_2 molecules in aqueous solution into highly active $^\bullet O_2^-$ radical (reaction (8)), then the $^\bullet O_2^-$ and $^\bullet OH^-$ radicals further react with RhB or BPA aqueous solution to degrade it into H_2O, CO_2, and small molecules (reaction (9)). Moreover, the unique 3D morphology of BOC/BOI-3 will provide more catalytic centers and increase the active sites. Accordingly, BOC/BOI-3 shows enhanced photocatalytic performance for degrading RhB and BPA pollutants.

$$BOC + h\nu \rightarrow BOC^* \left(e^- + h^+\right), \qquad (4)$$

$$BOI + h\nu \rightarrow BOI^* \left(e^- + h^+\right), \tag{5}$$

$$BOC^*\left(e^- + h^+\right) + BOI\left(e^- + h^+\right) \rightarrow BOC^*\left(h^+\right) + BOI^*\left(e^-\right), \tag{6}$$

$$H_2O + h^+ \xrightarrow{+1.99 \text{ V}} {}^\bullet OH + H^+, \tag{7}$$

$$O_2 + e^- \xrightarrow{-0.33 \text{ V}} {}^\bullet O_2^-, \tag{8}$$

$$RhB/BPA + {}^\bullet OH/{}^\bullet O_2^- \rightarrow H_2O + CO_2 + \text{other decomposed products}, \tag{9}$$

4. Conclusions

In this study, a simple solvothermal growth technique was used to synthesize the 3D hierarchical BOC/BOI heterostructure photocatalyst. The heterostructure demonstrated direct Z-scheme photocatalytic behavior in the photocatalytic degradation of RhB and BPA. The 3D hierarchal morphology of BOC/BOI can increase active sites due to its high surface area, and can improve visible-light absorption via multiple reflections inside the sample. XPS and mechanistic studies proved the generation of an internal electric field from BOI to BOC at their interface, which contributed to Z-scheme transport of photogenerated charge carriers in the BOC/BOI heterojunction. Thus, the BOC/BOI sample demonstrated a higher reaction rate and a higher degradation efficiency than the bare BOC and BOI during RhB and BPA degradation. Radical trapping analysis showed that ${}^\bullet O_2^-$, and ${}^\bullet OH$ radicals played a crucial role in RhB and BPA degradation. Through LC–MS results of RhB and BPA during photodegradation, its mineralization and degradation pathway were proposed. Therefore, the excellent photocatalytic performances of BOC/BOI are attributed to its large surface area, visible-light absorption, and low electron–hole recombination, which are due to its unique 3D hierarchical morphology and the direct Z-scheme photocatalytic process. Conclusively, direct Z-scheme BOC/BOI heterostructure is a suitable photocatalyst for use in the photodegradation of environmental pollutants.

Supplementary Materials: The following supporting information can be downloaded at: https://www.mdpi.com/article/10.3390/nano12050767/s1, Figure S1: Steps involved in the synthesis of heterostructure BOC/BOI composite; Figure S2: TGA and DSC plot of BiOI photocatalyst; Figure S3: Intensity line profiles of the inverse FFT of (a,b) BOC and BOI (c) in the BOC/BOI heterostructure; Figure S4: FESEM image of (a) BOC/BOI-3 composite and (b) its corresponding EDS sum image consists of four different colors: light red, dark red, green, and blue; these denote the presence of (c) Bi, (d) O, (e) Cl, and (f) I in the BOC/BOI-3 heterostructure, respectively (g) EDS spectrum of BOC/BOI-3 composite, with the inset table showing the atomic and elemental weight percentages of BOC/BOI-3 nano composite; Figure S5: XPS survey spectra for BOC, BOI, and BOC/BOI-based photocatalysts; Figure S6: Time-resolved absorption spectra of RhB degradation with (a) BOC, (b) BOI, (c) BOC/BOI-1, (d) BOC/BOI-2, (e) BOC/BOI-3, and (f) BOC/BOI-4 photocatalysts; Figure S7: Pseudo-first-order reaction kinetic plots of BOC, BOI, BOC/BOI-1, BOC/BOI-2, BOC/BOI-3, and BOC/BOI-4 photocatalyst for RhB degradation; Figure S8: Time-resolved absorption spectra of RhB degradation with (a) BOC, (b) BOI,(c) BOC-BOI-3, and (d) Pseudo-first-order reaction kinetic plots of BOI, BOC, and BOC/BOI-3; Figure S9: (a) Degradation efficiency with reaction rate constant and (b) 1st order reaction kinetics plot of RhB with and without scavengers in the presence of BOC/BOI-3; Figure S10: NBT degradation in the presence of (a) BOC, (b) BOI, and (c) BOC/BOI-3; (d) Chemical reaction for conversion of p-Nitroblue tetrazolium Chloride (NBT) to Formazan in the presence of super-oxide radicals (${}^\bullet O_2^-$); Figure S11: LC–MS of (a) RhB and (b) BPA after various photocatlytic reaction time; Figure S12: FESEM images BOC/BOI-3 heterostructures after (a) RhB and (b) BPA degradation; Table S1: Obtained parameters from the TRPL curves; Table S2: Comparison of photocatalytic degradation of RhB with recently reported literature; Table S3: Comparison of photocatalytic degradation of BPA with recently reported literature. References [15,16,26,37,56–84] are cited in the Supplementary Materials.

Author Contributions: S.T.U.D. contributed to the main idea and writing original draft. H.L. performed data analysis and curation. W.Y. contributed writing—review and editing. All authors have read and agreed to the published version of the manuscript.

Institutional Review Board Statement: Not applicable.

Informed Consent Statement: Not applicable.

Data Availability Statement: Not applicable.

References

1. Al-Buriahi, A.K.; Al-Gheethi, A.A.; Senthil Kumar, P.; Radin Mohamed, R.M.S.; Yusof, H.; Alshalif, A.F.; Khalifa, N.A. Elimination of Rhodamine B from Textile Wastewater Using Nanoparticle Photocatalysts: A Review for Sustainable Approaches. *Chemosphere* **2022**, *287*, 132162. [CrossRef] [PubMed]
2. Skjolding, L.M.; Jørgensen, L.v.G.; Dyhr, K.S.; Köppl, C.J.; McKnight, U.S.; Bauer-Gottwein, P.; Mayer, P.; Bjerg, P.L.; Baun, A. Assessing the Aquatic Toxicity and Environmental Safety of Tracer Compounds Rhodamine B and Rhodamine WT. *Water Res.* **2021**, *197*, 117109. [CrossRef]
3. Corrales, J.; Kristofco, L.A.; Steele, W.B.; Yates, B.S.; Breed, C.S.; Williams, E.S.; Brooks, B.W. Global Assessment of Bisphenol A in the Environment: Review and Analysis of Its Occurrence and Bioaccumulation. *Dose-Response* **2015**, *13*, 1559325815598308. [CrossRef] [PubMed]
4. Wright-Walters, M.; Volz, C.; Talbott, E.; Davis, D. An Updated Weight of Evidence Approach to the Aquatic Hazard Assessment of Bisphenol A and the Derivation a New Predicted No Effect Concentration (Pnec) Using a Non-Parametric Methodology. *Sci. Total Environ.* **2011**, *409*, 676–685. [CrossRef]
5. Lahrich, S.; Laghrib, F.; Farahi, A.; Bakasse, M.; Saqrane, S.; El Mhammedi, M.A. Review on the Contamination of Wastewater by COVID-19 Virus: Impact and Treatment. *Sci. Total Environ.* **2021**, *751*, 142325. [CrossRef]
6. Zhou, N.; Tan, J.; Li, X.; Wang, L.; Jin, C.; Chen, M.; Yu, Z.; Liang, Y.; Qiu, Z.; Li, W.; et al. Fabrication of Z-Scheme Bi5O7I/MIL-53(Fe) Hybrid with Improved Photocatalytic Performance under Visible Light Irradiation. *J. Mater. Sci. Mater. Electron.* **2020**, *31*, 4822–4835. [CrossRef]
7. Li, M.; Li, Y.; Chen, F.; Lin, X.; Feng, Q. Electrically Enhanced Photocatalysis for Gas-Phase Benzaldehyde Degradation by Ordered Mesoporous Titania/Conductive Carbon Felts. *Electrochim. Acta* **2016**, *216*, 517–527. [CrossRef]
8. Yuan, L.; Jiang, S.-M.; Li, Z.-Z.; Zhu, Y.; Yu, J.; Li, L.; Li, M.-Z.; Tang, S.; Sheng, R.-R. Photocatalyzed Cascade Meerwein Addition/Cyclization of N-Benzylacrylamides toward Azaspirocycles. *Org. Biomol. Chem.* **2018**, *16*, 2406–2410. [CrossRef]
9. Sharma, K.; Dutta, V.; Sharma, S.; Raizada, P.; Hosseini-Bandegharaei, A.; Thakur, P.; Singh, P. Recent Advances in Enhanced Photocatalytic Activity of Bismuth Oxyhalides for Efficient Photocatalysis of Organic Pollutants in Water: A Review. *J. Ind. Eng. Chem.* **2019**, *78*, 1–20. [CrossRef]
10. Tang, S.; Fu, Z.; Li, Y.; Li, Y. Study on Boron and Fluorine-Doped C_3N_4 as a Solid Activator for Cyclohexane Oxidation with H_2O_2 Catalyzed by 8-Quinolinolato IronIII Complexes under Visible Light Irradiation. *Appl. Catal. A Gen.* **2020**, *590*, 117342. [CrossRef]
11. Wu, X.; Zhang, Y.; Wang, K.; Zhang, S.; Qu, X.; Shi, L.; Du, F. In-Situ Construction of Bi/Defective Bi_4NbO_8Cl for Non-Noble Metal Based Mott-Schottky Photocatalysts towards Organic Pollutants Removal. *J. Hazard. Mater.* **2020**, *393*, 122408. [CrossRef] [PubMed]
12. Liang, C.; Lu, Z.-A.; Wu, J.; Chen, M.-X.; Zhang, Y.; Zhang, B.; Gao, G.-L.; Li, S.; Xu, P. Recent Advances in Plasmon-Promoted Organic Transformations Using Silver-Based Catalysts. *ACS Appl. Mater. Interfaces* **2020**, *12*, 54266–54284. [CrossRef] [PubMed]
13. Xiao, L.; Zhang, Q.; Chen, P.; Chen, L.; Ding, F.; Tang, J.; Li, Y.-J.; Au, C.-T.; Yin, S.-F. Copper-Mediated Metal-Organic Framework as Efficient Photocatalyst for the Partial Oxidation of Aromatic Alcohols under Visible-Light Irradiation: Synergism of Plasmonic Effect and Schottky Junction. *Appl. Catal. B Environ.* **2019**, *248*, 380–387. [CrossRef]
14. Xiong, S.; Yin, Z.; Zhou, Y.; Peng, X.; Yan, W.; Liu, Z.; Zhang, X. The Dual-Frequency (20/40 KHz) Ultrasound Assisted Photocatalysis with the Active Carbon Fiber-Loaded Fe^{3+}-TiO_2 as Photocatalyst for Degradation of Organic Dye. *Bull. Korean Chem. Soc.* **2013**, *34*, 3039–3045. [CrossRef]
15. Ma, Y.; Chen, Y.; Feng, Z.; Zeng, L.; Chen, Q.; Jin, R.; Lu, Y.; Huang, Y.; Wu, Y.; He, Y. Preparation, Characterization of Bi_3O_4Cl/g-C_3N_4 Composite and Its Photocatalytic Activity in Dye Degradation. *J. Water Process. Eng.* **2017**, *18*, 65–72. [CrossRef]
16. Wang, H.; Xu, L.; Liu, C.; Jiang, Z.; Feng, Q.; Wu, T.; Wang, R. A Novel Magnetic Photocatalyst Bi_3O_4Cl/$SrFe_{12}O_{19}$: Fabrication, Characterization and Its Photocatalytic Activity. *Ceram. Int.* **2020**, *46*, 460–467. [CrossRef]
17. Li, H.; Tu, W.; Zhou, Y.; Zou, Z. Z-Scheme Photocatalytic Systems for Promoting Photocatalytic Performance: Recent Progress and Future Challenges. *Adv. Sci.* **2016**, *3*, 1500389. [CrossRef]
18. Gu, W.; Xu, J.; Teng, F.; Ul Abideen, Z. Investigation on the Different Photocatalytic Properties of Bismuths Oxychlorides: $Bi_{12}O_{15}C_{16}$ versus Bi_3O_4Cl versus BiOCl. *ChemistrySelect* **2018**, *3*, 10721–10726. [CrossRef]
19. Di, J.; Xia, J.; Li, H.; Guo, S.; Dai, S. Bismuth Oxyhalide Layered Materials for Energy and Environmental Applications. *Nano Energy* **2017**, *41*, 172–192. [CrossRef]

20. Huang, H.; Xiao, K.; He, Y.; Zhang, T.; Dong, F.; Du, X.; Zhang, Y. In Situ Assembly of BiOI@Bi₁₂O₁₇Cl₂ P-n Junction: Charge Induced Unique Front-Lateral Surfaces Coupling Heterostructure with High Exposure of BiOI {001} Active Facets for Robust and Nonselective Photocatalysis. *Appl. Catal. B Environ.* **2016**, *199*, 75–86. [CrossRef]

21. Jin, X.; Ye, L.; Xie, H.; Chen, G. Bismuth-Rich Bismuth Oxyhalides for Environmental and Energy Photocatalysis. *Coord. Chem. Rev.* **2017**, *349*, 84–101. [CrossRef]

22. Cheng, L.; Xiao, X.; Wang, Y.; Lu, M. Fabrication of Microsphere-like Bi₃O₄Cl/BiOI Z-Scheme Heterostructure Composites and Its Enhanced Photocatalytic Performance for Degradation of MO and RhB. *Res. Chem. Intermed.* **2020**, *46*, 4685–4704. [CrossRef]

23. Yang, N.; Lv, X.; Zhong, S.; Qian, D.; Han, S.; Li, D.; Geng, X.; Fang, H.; Jiang, W. Preparation of Z-Scheme AgI/Bi₅O₇I Plate with High Visible Light Photocatalytic Performance by Phase Transition and Morphological Transformation of BiOI Microspheres at Room Temperature. *Dalton Trans.* **2018**, *47*, 11420–11428. [CrossRef]

24. Zhao, X.; You, Y.; Huang, S.; Wu, Y.; Ma, Y.; Zhang, G.; Zhang, Z. Z-scheme Photocatalytic Production of Hydrogen Peroxide over Bi₄O₅Br₂/g-C₃N₄ Heterostructure under Visible Light. *Appl. Catal. B Environ.* **2020**, *278*, 119251. [CrossRef]

25. Jiang, E.; Song, N.; Zhang, X.; Yang, L.; Liu, C.; Dong, H. In-Situ Fabrication of Z-Scheme Bi₃O₄Cl/Bi₁₂O₁₇Cl₂ Heterostructure by Facile PH Control Strategy to Boost Removal of Various Pollutants in Water. *Chem. Eng. J.* **2020**, *388*, 123483. [CrossRef]

26. Che, H.; Che, G.; Dong, H.; Hu, W.; Hu, H.; Liu, C.; Li, C. Fabrication of Z-Scheme Bi₃O₄Cl/g-C₃N₄ 2D/2D Heterojunctions with Enhanced Interfacial Charge Separation and Photocatalytic Degradation Various Organic Pollutants Activity. *Appl. Surf. Sci.* **2018**, *455*, 705–716. [CrossRef]

27. Wang, W.; Yu, J.C.; Shen, Z.; Chan, D.K.L.; Gu, T. G-C₃N₄ Quantum Dots: Direct Synthesis, Upconversion Properties and Photocatalytic Application. *Chem. Commun.* **2014**, *50*, 10148–10150. [CrossRef]

28. Ghoreishian, S.M.; Ranjith, K.S.; Lee, H.; Park, B.; Norouzi, M.; Nikoo, S.Z.; Kim, W.-S.; Han, Y.-K.; Huh, Y.S. Tuning the Phase Composition of 1D TiO₂ by Fe/Sn Co-Doping Strategy for Enhanced Visible-Light-Driven Photocatalytic and Photoelectrochemical Performances. *J. Alloy. Compd.* **2021**, *851*, 156826. [CrossRef]

29. Kumari, P.; Bahadur, N.; O'Dell, L.A.; Kong, L.; Sadek, A.; Merenda, A.; Dumée, L.F. Nanoscale 2D Semi-Conductors—Impact of Structural Properties on Light Propagation Depth and Photocatalytic Performance. *Sep. Purif. Technol.* **2021**, *258*, 118011. [CrossRef]

30. Liu, X.; Yang, Z.; Zhang, L. In-Situ Fabrication of 3D Hierarchical Flower-like β-Bi₂O₃@CoO Z-Scheme Heterojunction for Visible-Driven Simultaneous Degradation of Multi-Pollutants. *J. Hazard. Mater.* **2021**, *403*, 123566. [CrossRef]

31. Cheng, T.; Gao, H.; Liu, G.; Pu, Z.; Wang, S.; Yi, Z.; Wu, X.; Yang, H. Preparation of Core-Shell Heterojunction Photocatalysts by Coating CdS Nanoparticles onto Bi₄Ti₃O₁₂ Hierarchical Microspheres and Their Photocatalytic Removal of Organic Pollutants and Cr(VI) Ions. *Colloids Surf. A Physicochem. Eng. Asp.* **2022**, *633*, 127918. [CrossRef]

32. Lukic, S.; Menze, J.; Weide, P.; Busser, G.W.; Winterer, M.; Muhler, M. Decoupling the Effects of High Crystallinity and Surface Area on the Photocatalytic Overall Water Splitting over β-Ga₂O₃ Nanoparticles by Chemical Vapor Synthesis. *ChemSusChem* **2017**, *10*, 4190–4197. [CrossRef] [PubMed]

33. Jiang, E.; Liu, X.; Che, H.; Liu, C.; Dong, H.; Che, G. Visible-Light-Driven Ag/Bi₃O₄Cl Nanocomposite Photocatalyst with Enhanced Photocatalytic Activity for Degradation of Tetracycline. *RSC Adv.* **2018**, *8*, 37200–37207. [CrossRef]

34. Zhang, Y.; Zhu, G.; Gao, J.; Zhu, R.; Hojamberdiev, M.; Wei, X.; Liu, P. Synthesis of Plasmonic Enhance Sphere-like Ag/AgI/Bi₅O₇I Photocatalysts with Improved Visible-Light Responsive Activity under LED Light Irradiation. *J. Mater. Sci. Mater. Electron.* **2017**, *28*, 5460–5471. [CrossRef]

35. Rameshbabu, R.; Sandhiya, M.; Sathish, M. Fe (III) Ions Grafted Bismuth Oxychloride Nanosheets for Enhanced Electrochemical Supercapacitor Application. *J. Electroanal. Chem.* **2020**, *862*, 113958. [CrossRef]

36. Mihailova, B.; Gospodinov, M.; Konstantinov, L. Raman Spectroscopy Study of Sillenites. I. Comparison between Bi₁₂(Si,Mn)O₂₀ Single Crystals. *J. Phys. Chem. Solids* **1999**, *60*, 1821–1827. [CrossRef]

37. Chen, R.; Chen, Z.; Ji, M.; Chen, H.; Liu, Y.; Xia, J.; Li, H. Enhanced Reactive Oxygen Species Activation for Building Carbon Quantum Dots Modified Bi₅O₇I Nanorod Composites and Optimized Visible-Light-Response Photocatalytic Performance. *J. Colloid Interface Sci.* **2018**, *532*, 727–737. [CrossRef] [PubMed]

38. Chang, C.; Yang, H.; Mu, W.; Cai, Y.; Wang, L.; Yang, L.; Qin, H. In Situ Fabrication of Bismuth Oxyiodide (Bi₇O₉I₃/Bi₅O₇I) n-n Heterojunction for Enhanced Degradation of Triclosan (TCS) under Simulated Solar Light Irradiation. *Appl. Catal. B Environ.* **2019**, *254*, 647–658. [CrossRef]

39. Xiao, X.; Lin, Y.; Pan, B.; Fan, W.; Huang, Y. Photocatalytic Degradation of Methyl Orange by BiOI/Bi₄O₅I₂ Microspheres under Visible Light Irradiation. *Inorg. Chem. Commun.* **2018**, *93*, 65–68. [CrossRef]

40. Xu, B.; Gao, Y.; Li, Y.; Liu, S.; Lv, D.; Zhao, S.; Gao, H.; Yang, G.; Li, N.; Ge, L. Synthesis of Bi₃O₄Cl Nanosheets with Oxygen Vacancies: The Effect of Defect States on Photocatalytic Performance. *Appl. Surf. Sci.* **2020**, *507*, 144806. [CrossRef]

41. Fujimoto, A.; Yamada, Y.; Koinuma, M.; Sato, S. Origins of sp³C Peaks in C₁ₛ X-Ray Photoelectron Spectra of Carbon Materials. *Anal. Chem.* **2016**, *88*, 6110–6114. [CrossRef] [PubMed]

42. Ma, C.; Lee, J.; Kim, Y.; Cheol Seo, W.; Jung, H.; Yang, W. Rational Design of α-Fe₂O₃ Nanocubes Supported BiVO₄ Z-Scheme Photocatalyst for Photocatalytic Degradation of Antibiotic under Visible Light. *J. Colloid Interface Sci.* **2021**, *581*, 514–522. [CrossRef] [PubMed]

43. Dinh, C.-T.; Jain, A.; de Arquer, F.P.G.; De Luna, P.; Li, J.; Wang, N.; Zheng, X.; Cai, J.; Gregory, B.Z.; Voznyy, O.; et al. Multi-Site Electrocatalysts for Hydrogen Evolution in Neutral Media by Destabilization of Water Molecules. *Nat. Energy* **2019**, *4*, 107–114. [CrossRef]

44. Zhu, G.; Hojamberdiev, M.; Zhang, S.; Din, S.T.U.; Yang, W. Enhancing Visible-Light-Induced Photocatalytic Activity of BiOI Microspheres for NO Removal by Synchronous Coupling with Bi Metal and Graphene. *Appl. Surf. Sci.* **2019**, *467–468*, 968–978. [CrossRef]

45. Yao, C.; Wang, X.; Zhao, W.; Li, T.; He, Y.; Ran, X.; Guo, L. Probing the Facet-Dependent Intermediate in the Visible-Light Degradation of RhB by Carbon-Coated Anatase TiO_2 Nanoparticles. *J. Alloy. Compd.* **2020**, *846*, 156335. [CrossRef]

46. Zhu, G.; Hojamberdiev, M.; Zhang, W.; Taj Ud Din, S.; Joong Kim, Y.; Lee, J.; Yang, W. Enhanced Photocatalytic Activity of Fe-Doped $Bi_4O_5Br_2$ Nanosheets Decorated with Au Nanoparticles for Pollutants Removal. *Appl. Surf. Sci.* **2020**, *526*, 146760. [CrossRef]

47. Huang, J.; Dou, L.; Li, J.; Zhong, J.; Li, M.; Wang, T. Excellent Visible Light Responsive Photocatalytic Behavior of N-Doped TiO_2 toward Decontamination of Organic Pollutants. *J. Hazard. Mater.* **2021**, *403*, 123857. [CrossRef]

48. Xie, Y.; Li, P.; Zeng, Y.; Li, X.; Xiao, Y.; Wang, Y.; Zhang, Y. Thermally Treated Fungal Manganese Oxides for Bisphenol A Degradation Using Sulfate Radicals. *Chem. Eng. J.* **2018**, *335*, 728–736. [CrossRef]

49. Ullah, R.; Zheng, Y. Raman Spectroscopy of 'Bisphenol A'. *J. Mol. Struct.* **2016**, *1108*, 649–653. [CrossRef]

50. Huang, S.; Wang, C.; Sun, H.; Wang, X.; Su, Y. Steering Charge Kinetics of Tin Niobate Photocatalysts: Key Roles of Phase Structure and Electronic Structure. *Nanoscale Res. Lett.* **2018**, *13*, 1–12. [CrossRef] [PubMed]

51. Huang, L.; Yang, L.; Li, Y.; Wang, C.; Xu, Y.; Huang, L.; Song, Y. P-n $BiOI/Bi_3O_4Cl$ Hybrid Junction with Enhanced Photocatalytic Performance in Removing Methyl Orange, Bisphenol A, Tetracycline and Escherichia Coli. *Appl. Surf. Sci.* **2020**, *527*, 146748. [CrossRef]

52. Li, Z.; Dong, H.; Wu, Z.; Shen, J.; Xu, D.; He, R.; Wan, L.; Zhang, S. Novel P-n Type Porous Ag_2O/Bi_5O_7I Heterojunction for Uv–Vis-NIR Activated High Efficient Photocatalytic Degradation of Bisphenol A: Photoelectric Properties and Degradation Mechanism. *Appl. Surf. Sci.* **2020**, *529*, 147162. [CrossRef]

53. Liu, Q.; Lu, Y.; Lin, S.; Hu, Y.; Tian, N.; Huang, H. Room-Temperature Controllable Synthesis of Bi_5O_7I Nanostrips for Improved Photocatalytic Activity. *Colloids Surf. A Physicochem. Eng. Asp.* **2020**, *594*, 124642. [CrossRef]

54. Hankin, A.; Alexander, J.C.; Kelsall, G.H. Constraints to the Flat Band Potential of Hematite Photo-Electrodes. *Phys. Chem. Chem. Phys.* **2014**, *16*, 16176–16186. [CrossRef] [PubMed]

55. Huang, H.; Xiao, K.; Tian, N.; Dong, F.; Zhang, T.; Du, X.; Zhang, Y. Template-Free Precursor-Surface-Etching Route to Porous, Thin $g-C_3N_4$ Nanosheets for Enhancing Photocatalytic Reduction and Oxidation Activity. *J. Mater. Chem. A* **2017**, *5*, 17452–17463. [CrossRef]

56. Mian, F.; Bottaro, G.; Rancan, M.; Pezzato, L.; Gombac, V.; Fornasiero, P.; Armelao, L. $Bi_{12}O_{17}Cl_2/(BiO)_2CO_3$ Nanocomposite Materials for Pollutant Adsorption and Degradation: Modulation of the Functional Properties by Composition Tailoring. *ACS Omega* **2017**, *2*, 6298–6308. [CrossRef] [PubMed]

57. Han, L.; Guo, Y.; Lin, Z.; Huang, H. 0D to 3D Controllable Nanostructures of BiOBr via a Facile and Fast Room-Temperature Strategy. *Colloids Surf. A Physicochem. Eng. Asp.* **2020**, *603*, 125233. [CrossRef]

58. Cui, B.; Cui, H.; Li, Z.; Dong, H.; Li, X.; Zhao, L.; Wang, J. Novel $Bi_3O_5I_2$ Hollow Microsphere and Its Enhanced Photocatalytic Activity. *Catalysts* **2019**, *9*, 709. [CrossRef]

59. Yu, C.; Fan, C.; Yu, J.C.; Zhou, W.; Yang, K. Preparation of Bismuth Oxyiodides and Oxides and Their Photooxidation Characteristic under Visible/UV Light Irradiation. *Mater. Res. Bull.* **2011**, *46*, 140–146. [CrossRef]

60. Liao, C.; Ma, Z.; Chen, X.; He, X.; Qiu, J. Controlled Synthesis of Bismuth Oxyiodide toward Optimization of Photocatalytic Performance. *Appl. Surf. Sci.* **2016**, *387*, 1247–1256. [CrossRef]

61. Sun, X.; Wu, J.; Li, Q.; Liu, Q.; Qi, Y.; You, L.; Ji, Z.; He, P.; Sheng, P.; Ren, J.; et al. Fabrication of $BiOIO_3$ with Induced Oxygen Vacancies for Efficient Separation of the Electron-Hole Pairs. *Appl. Catal. B Environ.* **2017**, *218*, 80–90. [CrossRef]

62. Mera, A.C.; Rodríguez, C.A.; Meléndrez, M.F.; Valdés, H. Synthesis and Characterization of BiOI Microspheres under Standardized Conditions. *J. Mater. Sci.* **2017**, *52*, 944–954. [CrossRef]

63. Long, M.; Hu, P.; Wu, H.; Chen, Y.; Tan, B.; Cai, W. Understanding the Composition and Electronic Structure Dependent Photocatalytic Performance of Bismuth Oxyiodides. *J. Mater. Chem. A* **2015**, *3*, 5592–5598. [CrossRef]

64. Huang, Y.; He, Y.; Cui, M.; Nong, Q.; Yu, J.; Wu, F.; Meng, X. Synthesis of $AgCl/Bi_3O_4Cl$ Composite and Its Photocatalytic Activity in RhB Degradation under Visible Light. *Catal. Commun.* **2016**, *76*, 19–22. [CrossRef]

65. Cui, M.; Yu, J.; Lin, H.; Wu, Y.; Zhao, L.; He, Y. In-Situ Preparation of Z-Scheme AgI/Bi_5O_7I Hybrid and Its Excellent Photocatalytic Activity. *Appl. Surf. Sci.* **2016**, *387*, 912–920. [CrossRef]

66. Geng, X.; Chen, S.; Lv, X.; Jiang, W.; Wang, T. Synthesis of $G-C_3N_4/Bi_5O_7I$ Microspheres with Enhanced Photocatalytic Activity under Visible Light. *Appl. Surf. Sci.* **2018**, *462*, 18–28. [CrossRef]

67. Liu, C.; Huang, H.; Du, X.; Zhang, T.; Tian, N.; Guo, Y.; Zhang, Y. In Situ Co-Crystallization for Fabrication of $g-C_3N_4/Bi_5O_7I$ Heterojunction for Enhanced Visible-Light Photocatalysis. *J. Phys. Chem. C* **2015**, *119*, 17156–17165. [CrossRef]

68. Luo, Y.; Zhang, M.; Yin, H.; Yao, J.; Chen, S.; Liu, X. One Pot Controllable Synthesis of Palygorskite/Bismuth Oxyiodide Hierarchical Microspheres for Improved Visible-Light Photocatalytic Performance. *Colloids Surf. A Physicochem. Eng. Asp.* **2019**, *578*, 123573. [CrossRef]

69. Zhao, Z.; Wang, M.; Yang, T.; Fang, M.; Zhang, L.; Zhu, H.; Tang, C.; Huang, Z. In Situ Co-Precipitation for the Synthesis of an Ag/AgBr/Bi_5O_7I Heterojunction for Enhanced Visible-Light Photocatalysis. *J. Mol. Catal. A Chem.* **2016**, *424*, 8–16. [CrossRef]

70. Bai, Y.; Shi, X.; Wang, P.; Wang, L.; Xie, H.; Li, Z.; Qu, L.; Ye, L. Synthesis of One-Dimensional $Bi_5O_7Br_{0.5}I_{0.5}$ Solid Solution for Effective Real Oilfield Wastewater Treatment via Exciton Photocatalytic Process. *J. Taiwan Inst. Chem. Eng.* **2018**, *91*, 358–368. [CrossRef]

71. Feng, S.; Du, H.; Xie, T.; Xu, L.; Wang, Y. Preparation and Photocatalytic Activity of BiOI/$MnxZn1-XFe_2O_4$ Magnetic Photocatalyst. *Ceram. Int.* **2019**, *45*, 10468–10474. [CrossRef]

72. Huang, H.; Xiao, K.; Zhang, T.; Dong, F.; Zhang, Y. Rational Design on 3D Hierarchical Bismuth Oxyiodides via in Situ Self-Template Phase Transformation and Phase-Junction Construction for Optimizing Photocatalysis against Diverse Contaminants. *Appl. Catal. B Environ.* **2017**, *203*, 879–888. [CrossRef]

73. Chang, F.; Yan, W.; Wang, X.; Peng, S.; Li, S.; Hu, X. Strengthened Photocatalytic Removal of Bisphenol a by Robust 3D Hierarchical N-p Heterojunctions $Bi_4O_5Br_2$-MnO_2 via Boosting Oxidative Radicals Generation. *Chem. Eng. J.* **2022**, *428*, 131223. [CrossRef]

74. Liu, Y.; Zhu, G.; Gao, J.; Zhu, R.; Hojamberdiev, M.; Wang, C.; Wei, X.; Liu, P. A Novel Synergy of Er^{3+}/Fe^{3+} Co-Doped Porous Bi_5O_7I Microspheres with Enhanced Photocatalytic Activity under Visible-Light Irradiation. *Appl. Catal. B Environ.* **2017**, *205*, 421–432. [CrossRef]

75. Cao, C.-S.; Wang, J.; Yu, X.; Zhang, Y.; Zhu, L. Photodegradation of Seven Bisphenol Analogues by Bi_5O_7I/UiO-67 Heterojunction: Relationship between the Chemical Structures and Removal Efficiency. *Appl. Catal. B Environ.* **2020**, *277*, 119222. [CrossRef]

76. Guo, Y.; Nan, J.; Xu, Y.; Cui, F.; Shi, W.; Zhu, Y. Thermodynamic and Dynamic Dual Regulation $Bi_2O_2CO_3$/Bi_5O_7I Enabling High-Flux Photogenerated Charge Migration for Enhanced Visible-Light-Driven Photocatalysis. *J. Mater. Chem. A* **2020**, *8*, 10252–10259. [CrossRef]

77. Zhao, C.; Wang, J.; Chen, X.; Wang, Z.; Ji, H.; Chen, L.; Liu, W.; Wang, C.-C. Bifunctional $Bi_{12}O_{17}Cl_2$/MIL-100(Fe) Composites toward Photocatalytic Cr(VI) Sequestration and Activation of Persulfate for Bisphenol A Degradation. *Sci. Total Environ.* **2021**, *752*, 141901. [CrossRef]

78. Gu, J.; Yu, Y.; Chen, S.; Shi, W.; Wang, Y.; Liao, Y.; Chen, H.; Jiang, F. Heterojunction Photocatalyst of Cavity Shaped Bi_2S_3/g-C_3N_4 for Bisphenol a Degradation: Regulation of Internal Electric Field via Assistance of Interfacial Functional Groups. *Chem. Eng. J.* **2021**, *424*, 130539. [CrossRef]

79. He, X.; Wu, M.; Ao, Z.; Lai, B.; Zhou, Y.; An, T.; Wang, S. Metal–Organic Frameworks Derived C/TiO_2 for Visible Light Photocatalysis: Simple Synthesis and Contribution of Carbon Species. *J. Hazard. Mater.* **2021**, *403*, 124048. [CrossRef] [PubMed]

80. Feng, H.; Liang, L.; Wu, W.; Huang, Z.; Liu, Y. Architecting Epitaxial-Lattice-Mismatch-Free (LMF) Zinc Oxide/Bismuth Oxyiodide Nano-Heterostructures for Efficient Photocatalysis. *J. Mater. Chem. C* **2020**, *8*, 11263–11273. [CrossRef]

81. Zhao, K.; Zhang, Z.; Feng, Y.; Lin, S.; Li, H.; Gao, X. Surface Oxygen Vacancy Modified Bi_2MoO_6/MIL-88B(Fe) Heterostructure with Enhanced Spatial Charge Separation at the Bulk & Interface. *Appl. Catal. B Environ.* **2020**, *268*, 118740. [CrossRef]

82. Fei, H.; Shao, J.; Li, H.; Li, N.; Chen, D.; Xu, Q.; He, J.; Lu, J. Construction of Ultra-Thin 2D CN-$Br_{0.12}$/2%RhOx Photo-Catalyst with Rapid Electron and Hole Separation for Efficient Bisphenol A Degradation. *Appl. Catal. B Environ.* **2021**, *299*, 120623. [CrossRef]

83. Kuila, A.; Saravanan, P.; Bahnemann, D.; Wang, C. Novel Ag Decorated, BiOCl Surface Doped $AgVO_3$ Nanobelt Ternary Composite with Z-Scheme Homojunction-Heterojunction Interface for High Prolific Photo Switching, Quantum Efficiency and Hole Mediated Photocatalysis. *Appl. Catal. B Environ.* **2021**, *293*, 120224. [CrossRef]

84. Yin, S.; Chen, R.; Ji, M.; Jiang, Q.; Li, K.; Chen, Z.; Xia, J.; Li, H. Construction of Ultrathin MoS_2/Bi_5O_7I Composites: Effective Charge Separation and Increased Photocatalytic Activity. *J. Colloid Interface Sci.* **2020**, *560*, 475–484. [CrossRef] [PubMed]